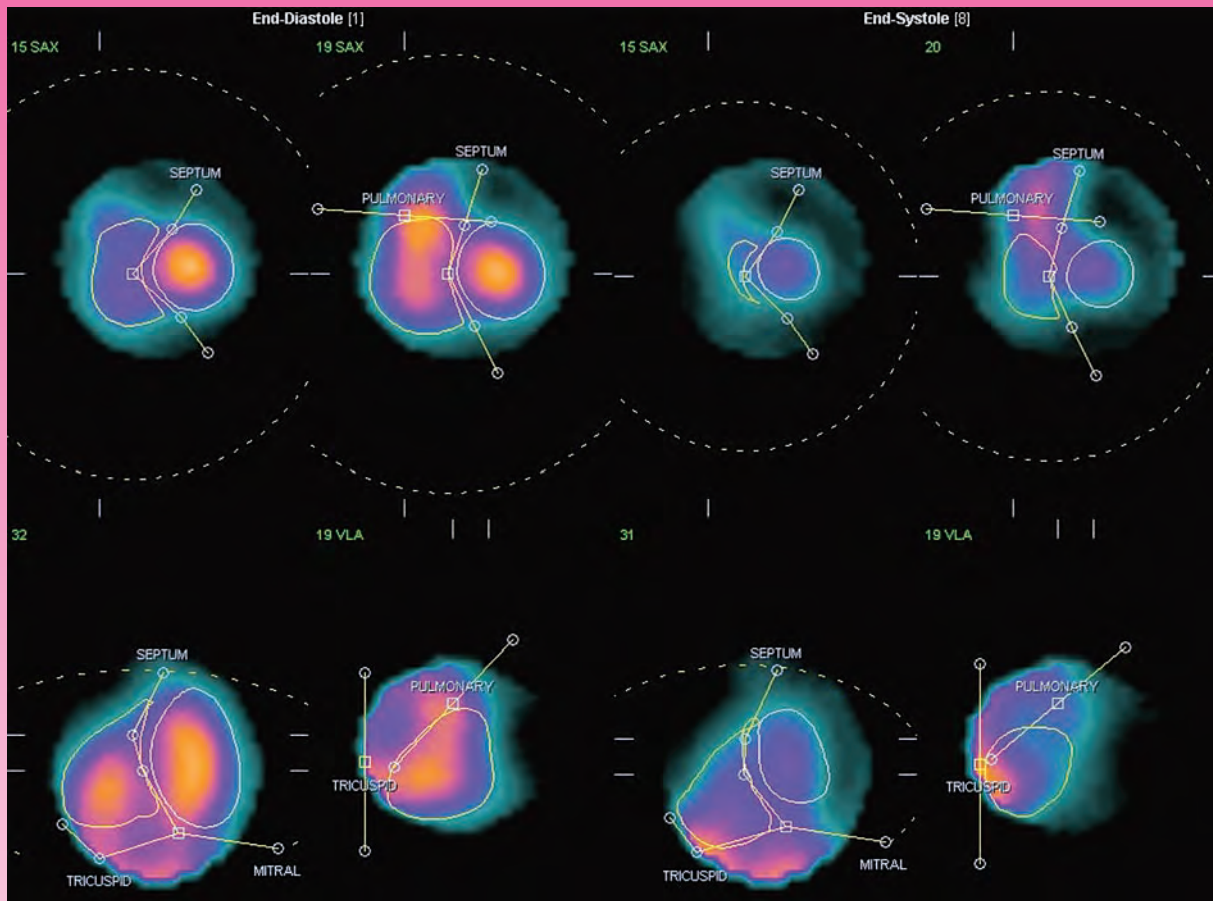


核醫技術學雜誌

Journal of Nuclear Medicine Technology



QBS 軟體允許透過在 LV 上移動橢圓手柄，來手動調整 LV 和 RV 之 ROI

Volume 19 Number 1

December 2022

第十九卷 第一期

中華民國一十一年十二月

Published by NM Technology Committee, the Society of Nuclear Medicine, R.O.C.

中華民國核醫學學會
醫技委員會 發行

核醫技術學雜誌

Journal of Nuclear Medicine Technology

發行人 (Publisher)

王昱豐 (Yuh-Feng Wang)
台北榮民總醫院

創刊人 (Original Publisher)

黃延城 (Yan-Cherng Huang)
台北榮民總醫院

總編輯 (Editor-in-Chief)

杜高瑩 (Kao-Ying Tu)
台北馬偕紀念醫院

副總編輯 (Associate Editors-in-Chief)

楊邦宏 (Bang-Hung Yang)
台北榮民總醫院

執行秘書 (Production Secretary)

王秀珊 (Hsiu-Shan Wang)
台北三軍總醫院

編輯委員 (Editorial Board)

北區

陳恩賜 (En-Shih Cheng)
三軍總醫院

王安美 (An-Mei Wang)
台北馬偕醫院

黃奕琿 (Yih-Hwen Huang)
台大醫院

蔡佳玲 (Chia-Lin Tsai)
長庚醫院

辜啓泰 (Chi-Tai Ku)

新光醫院

梁瑋玲 (Wei-Ling Liang)
和信醫院

黃馨美 (Hsing-Mei Huang)
國泰醫院

吳璧珊 (Pi-Shan Wu)
市立聯合醫院

陳雅鳳 (Ya-Huang Chen)
亞東醫院

黃雅婕 (Ya-Chieh Huang)
萬芳醫院

陳惠萍 (Hui-Ping Chen)
聯新國際醫院

郭俊良 (Chun-Liang Kuo)
新竹馬偕醫院

中區

周國堂 (Kuo-Tang Chou)
台中榮民總醫院

顏國揚 (Kuo-Yang Yen)
中國醫學大學附設醫院

張白容 (Pai-Jung Chang)
中山醫學大學附設醫院

姜繼宗 (Chi-Tsung Chiang)
中國醫學大學附設醫院

黃政凱 (Cheng-Kai Huang)
中港澄清醫院

陳逸珊 (Yi-Shan Chen)
台中慈濟醫院

詹況栗 (Kuang-Li Chang)
國軍台中總醫院

南區

張桂蘭 (Kuei-Lan Chang)
高雄醫學院附設醫院

李世昌 (Shih-Chang Li)
成大醫院

王文祥 (Wen-Hsiang Wang)
義大醫院

俞長青 (Chang-Ching Yu)
高雄榮民總醫院

鄭時維 (Shih-Wei Cheng)
屏東基督教醫院

莊欣慧 (Hsin-Hui Chuang)
國軍左營醫院

許幼青 (You-Ching Hsu)
嘉義慈濟醫院

張紫綺 (Tzu-Chi Chang)
柳營奇美醫院

核醫技術學雜誌

第 19 卷第 1 期

中華民國核醫學學會醫技委員會學誌

中華民國 111 年 12 月發行

原 著

- 使用平面和單光子電腦斷層技術執行放射性核種心室造影並探討
與心臟超音波報告之相關性..... 1
張紫綺 周詩瑾 洪佑昇
- 蓋格米勒計數器套件基本測試：計數統計與氟-18 衰減曲線計數..... 9
柴發順 江泰林 歐玲君 李正輝
- 不同材質防疫隔板的輻射屏蔽能力評估：蒙地卡羅模擬實驗..... 17
柴發順 江泰林 歐玲君 李正輝

病例報告

- 氟化去氧葡萄糖正子電腦斷層造影偵測腸胃道基質瘤..... 25
鄭如華 辜啓泰 陳遠光
- 利用進一步局部延遲像排除腸道有意外發現的局部 FDG 攝取—案例報告..... 31
吳麗君 楊淑琴 顏玉安 李將瑄
- 氟化去氧葡萄糖正子電腦斷層造影偵測早期腹部濾泡性淋巴瘤..... 37
林衍陸 林宋淑惠 陳遠光
- 大劑量 I-131 治療甲狀腺癌病人掃描時發現膽囊之偽陽性探討..... 43
朱秀蘭 顏維徵 紀雅閔 繆孝謙 游慧貞
-

Journal of Nuclear Medicine Technology

The Official Publication of NM Technology Committee, the Society
of Nuclear Medicine, R.O.C.

Volume 19, Number 1

ISSN 1818-2712
December 2022

Original Articles

- The Radionuclide Ventriculography Using Planar and SPECT
(Single Photon Emission Tomography) Techniques to Explore
the Correlation with Echocardiography 1**
Tzu-Chi Chang, Shih-Chin Chou, Yu-Sheng Hung
- Geiger-Müller Counter Kit Basic Test: Counting Statistics and Fluorine-18
Decay Curve Counting 9**
Fa-Shun Tsai, Tai-Lin Jiang, Lin-Chun Ou, Cheng-Hui Lee
- Evaluation of Radiation Shielding Ability of Different Materials
Anti-epidemic Partitions: Monte Carlo Experiment 17**
Fa-Shun Tsai, Tai-Lin Jiang, Lin-Chun Ou, Cheng-Hui Lee

Case Reports

- Intestine Gastrointestinal Stromal Tumor Detected by FDG PET/CT 25**
Ru-Hwa Cheng, Chi-Tai Ku, Yen-Kung Chen
- Excluded Incidental Finding of FDG Uptake in the Bowel using a Further
Delayed Image – A Case Report 31**
Li-Chun Wu, Shu-Chin Yang, Yu-An Yen, Chiang-Hsuan Lee
- Early Abdominal Follicular Lymphoma Detected by FDG PET/CT 37**
Yen-Lu Lin, Shu-Hui Lin-Sung, Yen-Kung Chen
- False Positive Uptake of Gallbladder on Whole Body Scan after High Dose Radioiodine
I-131 Therapy for Differentiated Thyroid Cancer 43**
Hsiu-Lan Chu, Wei-Jheng Yen, Ya-Min Chi, Hsiao-Chien Miao, Hui-Chen Yu
-

中華民國 93 年 11 月 20 日創刊

發行：中華民國核醫學學會
秘書處

理事長：王昱豐

醫技委員會：陳惠萍
主任委員

執行秘書：王秀珊

投稿信箱：susanwang@ndmctsggh.edu.tw

會址：112 台北市北投區石牌路二段 201 號
核醫部轉核醫學學會

電話：02-2875-7301 #587

電子信箱：tsnm.tw@gmail.com

劃撥帳號：19781819

戶名：中華民國核醫學學會

印刷：宇晨企業有限公司 yuchen68@ms51.hinet.net

地址：台北市和平東路二段 151 號 6 樓

電話：(02) 27037667 傳真：27033381

使用平面和單光子電腦斷層技術執行放射性核種心室造影 並探討與心臟超音波報告之相關性

張紫綺^{1,2} 周詩瑾¹ 洪佑昇^{1*}

¹ 奇美醫療財團法人柳營奇美醫院 核子醫學科

² 高雄醫學大學 醫學影像暨放射科學系

中文摘要

目的：並將心臟超音波作為 LVEF 的參考標準，了解平面和斷層造影何者與心臟超音波結果相關性較高。

材料與方法：收集 2015/08/10-2020/01/09 進行 MUGA 平面和 / 或斷層造影及心臟超音波的患者，且記錄每項檢查的 LVEF。靜脈注射 pyrophosphate 及 Tc-99m pertechnetate，再進行門控掃描。

使用西門子伽馬照相機取像，及 e-soft 軟體及 QBS 演算法計算 LVEF。且定義 LVEF 小於 50% 為陽性。利用 SPSS 及 Excel 進行資料分析。

結果：本研究有 54 名男性，12 名女性。平面造影與心臟超音波、斷層造影與心臟超音波測量出的平均 LVEF 值分別是 $43.20 \pm 13.64\%$ 與 47.66 ± 13.71 ， $45.2 \pm 21.43\%$ 與 47.19 ± 14.45 。

從平面與斷層造影得出的 LVEF 值皆顯示出與心臟超音波有相關性 (分別是 $r = 0.729$, $p < 0.001$, $r = 0.772$ ，與 $p < 0.001$)。平面與斷層造影兩者之檢查結果，皆與心臟超音波檢查結果相近。

結論：斷層造影可提供較多的臨床資訊且受人為干擾較少，目前臨床已常規使用斷層造影評估心室功能。

關鍵詞：心臟超音波 (echocardiography)、MUGA、平面造影、斷層造影

核醫技學誌 2022;19:1-7

接受日期：2022 年 4 月 28 日

通訊作者：洪佑昇

聯絡地址：台南市柳營區太康里 201 號 柳營奇美醫院核子醫學科

電話：06-6226999 轉 71042

電子郵件：ch5800@mail.chimei.org.tw

前言

心臟衰竭又稱為鬱血性心衰竭，是指心臟功能受損，心臟無法打出足夠的血流量，以滿足身體及組織代謝的所需求，而產生一連串的症狀，如呼吸困難、氣喘、運動耐力變差、疲倦及全身或四肢水腫，臨床檢查會發現有心臟肥大的情形。左心室射出分數 (Left Ventricular Ejection Fraction, LVEF) 和右心室射出分數 (Right Ventricular Ejection Fraction, RVEF) 以及左心室心室壁運動的精確測量，有助於鬱血性心衰竭 (Congestive heart failure, CHF) 患者的治療。

核醫心室功能檢查 (Ventricular function study) 主要經由測量心室射出率 (Ejection fraction, EF)、心室壁運動 (Ventricular wall motion)、功能性影像 (Functional image) 等定性及定量分析，評估心室整體的功能。臨床上心室功能檢查主要用於評估冠狀動脈疾病、心臟毒性、心肌病、瓣膜病等各種心臟疾病。這項檢查的特點是簡單、非侵襲性、客觀、及準確。核醫心室功能檢查方法主要有 Multigated Blood Pool (MUGA) 及 First-Pass 等兩種 [1]。

MUGA 檢查可動態分析心室壁運動，評估心室壁運動是否異常，例如運動機能減退 (Hypokinesia)、運動不能症 (Akinesia)、運動障礙 (Dyskinesia) 等。MUGA 檢查最重要是可計算 Global LVEF 及 RVEF [1]。

門控血池 SPECT (Gated blood pool SPECT) 易於執行，它可以透過斷層掃描來區分左心室和右心室，而不會與其他心腔重疊，能進行較精確的測量。並且允許進行複雜的心室壁運動分析，這些都可以在同一次檢查中完成 [1]。檢查結果可由定性及定量分析來判讀。主要是應用電腦計算心室每單位之搏出量、收縮幅度等，並以彩色圖形顯示其變化，經由顏色之變化能更準確的發現病灶位置。常用的功能性影像包括相位分析、振幅分

析、搏出量圖、Paradox image 等。另外亦可計算舒張末容積 (EDV)、收縮末容積 (ESV)、Peak filling rate、Time to peak filling rate 等及評估舒張功能 [1]。

本研究將心臟超音波作為左心室射出率 (Left Ventricular Ejection Fraction, LVEF) 的參考標準，了解平面造影及斷層造影何者與心臟超音波檢查結果相關性較高。

材料與方法

收集 2017/10/06-2020/07/23 之心臟血管內科病人之病歷資料，20 歲以上成人且不限性別，且須接受核醫及心臟超音波檢查，共有 66 名病人 (其中一名斷層與平面檢查皆有執行)。排除 20 歲以下，或缺少核醫及心臟超音波檢查之成人。執行平面造影人數為 33 名，斷層造影人數為 34 名 (表 3)。

檢查步驟

我們採用的檢查方式是靜態門控平衡放射性核素心室造影 (Rest gated equilibrium radionuclide ventriculography)。檢查前病人不需任何準備，使用的放射製劑為 Tc-99m labeled RBC。檢查的方法為先由靜脈注射 Pyrophosphate，30 分鐘後，由靜脈注射 20 mCi 的 Tc-99m pertechnetate，再經 10 分鐘即可進行掃描，掃描時間約十至二十分鐘。本研究經人體試驗委員會 (Institutional Review Board, IRB) 核准，IRB 案號為

11009-L05。

平面造影 (Planar image)

造影條件

使用西門子 E.CAM 伽馬照相機，搭配低能量高解析度準直儀，能窗為 15%、能峰為 140 keV。並利用單一探頭，角度為 LAO 45 度 (Best septal view)、每個心跳周期收取 16 Frames、矩陣大小為 128×128、放大倍率為兩倍，Beat window width 為 ±40%，整個取像過程約需十分鐘。

影像處理

使用西門子 e-soft 軟體手動或自動計算 LVEF。LVEF 可利用雙 ROI (Region of interest) 法得出，分別圈出背景及左心室之 ROI。背景 ROI 放置在靠近心室的位置，左心室的 ROI 則可自動或利用手動圈畫出左心室輪廓 (圖 1)。e-soft 軟體將舒張末期與收縮末期之左心室 ROI 內光子數扣除背景 ROI 光子數，並算得 LVEF。另外，在平面造影角度下 RV 會被擋住，因此 e-soft 無法評估 RV，而臨床實務上亦不需要針對 RV 去調角度。

斷層造影 (SPECT tomography image)

造影條件

斷層造影使用與平面造影相同的照相機，探頭角度為 180°，斷層造影參數包含了每 180°收取 30 張影像、

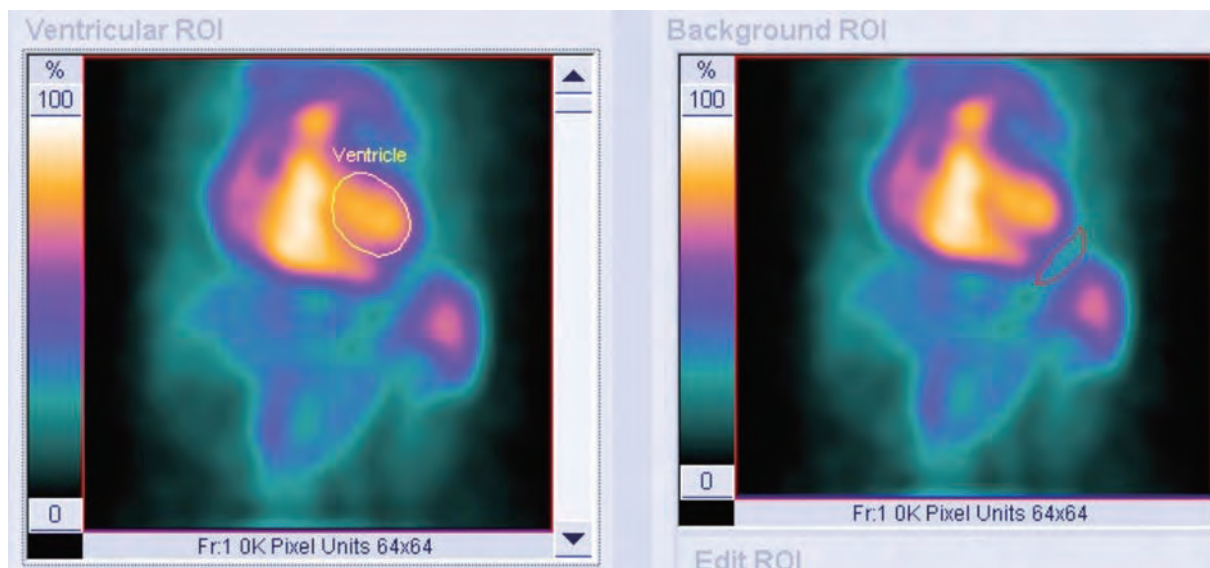


圖 1. MUGA 影像處理之雙 ROI 法

每張影像收 30 秒、每個心跳周期收取 16 Frames、矩陣大小為 64×64、放大倍率為 1.45 倍、Step and shoot mode、能窗為 15%、能峰為 140 keV，Beat window width 為 ±40%。

影像處理

使用 Cedars Sinai Quantitative Blood-Pool SPECT (QBS) software，影像利用反投影法重組，濾鏡為 Butterworth filter (cutoff 0.4, order 5)，並手動調整 ROI 產生短軸資料。

斷層造影使用全自動 QBS 演算法進行處理。如果無法識別心室邊界，QBS 軟體允許透過在 LV 上移動橢圓手柄來手動調整 LV 和 RV 之 ROI (圖 2)。因此，LVEF 是使用 LV 舒張末期和收縮末期的最大離散度圖像計算得出。對於 RVEF 計算，無需進一步調整 LV 和 RV ROI，即可根據 LV 相位得出 RV。在 LV 和 RV 之間發生相位差的情況下，使用視覺上最大分散的 RV 舒張末期和收縮末期圖像手動調整並計算出 RVEF [2]。

可利用舒張末期至收縮末期離散度的系列影像 (Cine) 及左右心室之運動極坐標圖，對 QBS 影像的左右心室運動進行評估，並允許操作人員將循環的電影旋轉到任何角度，以便對特定心臟區域進行最佳評估 [2]。亦提供左右心室的容積和充盈曲線、計算出的舒張參數、全心和局部直方圖以及相位分析頁面。

資料分析

利用 SPSS 統計軟體及 Excel 進行資料統整、相關分析。測量的平均值以平均值 ± 標準差 (Mean ± sd) 表示。使用相關分析斷層造影、平面造影及心臟超音波之 LVEF 結果。P 值小於 0.05 時，代表有統計意義。

皮爾森相關係數 (r)：

- 當 $r > 0$ 時，表示兩變數正相關， $r < 0$ 時，兩變數為負相關。
- $|r|$ 越接近 1，兩變數間線性關係越密切； $|r|$ 越接近於 0，表示兩變數的線性相關越弱。

一般可按三級劃分： $|r| < 0.3$ 為低度線性相關；0.3

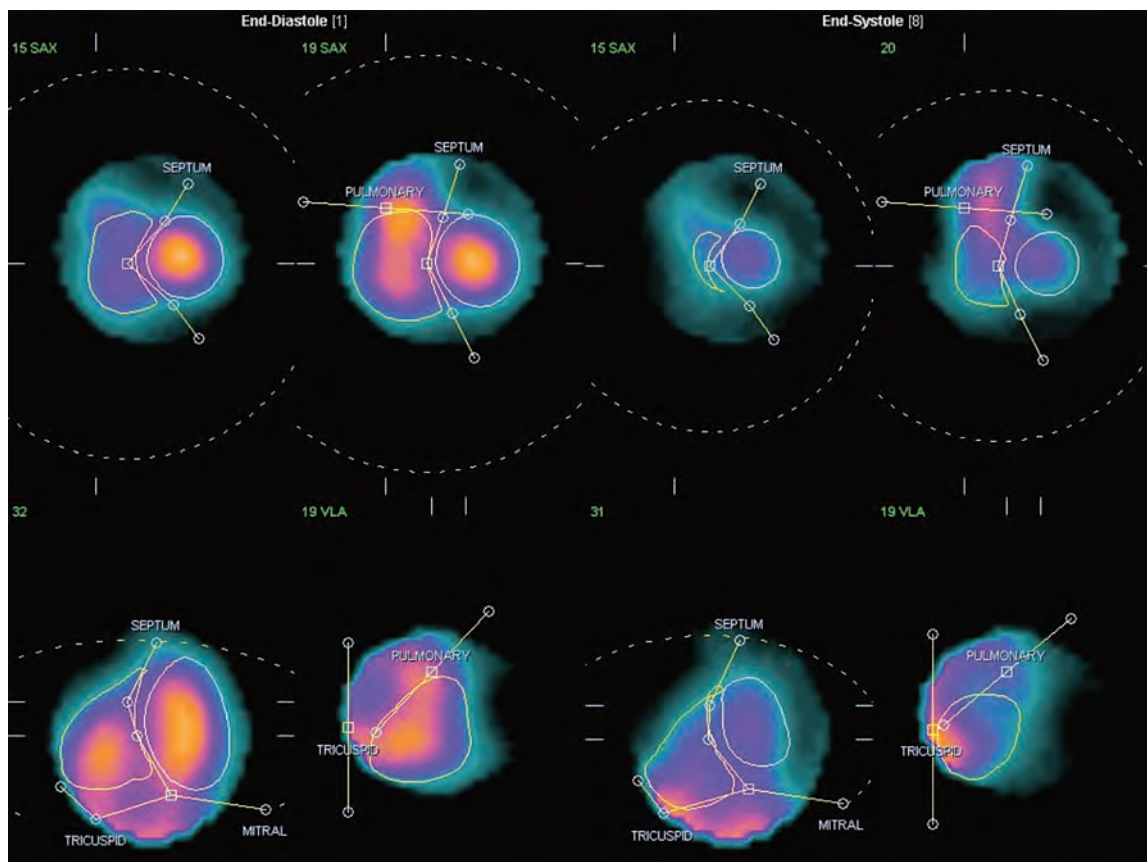


圖 2. QBS 軟體允許透過在 LV 上移動橢圓手柄，來手動調整 LV 和 RV 之 ROI

$\leq |r| < 0.7$ 為顯著性相關； $0.7 \leq |r| < 1$ 為高度線性相關。

分別分析平面造影與心臟超音波、斷層造影與心臟超音波之 LVEF 診斷結果，若核醫與心臟超音波檢查結果相同，亦即同為陽性 (LVEF 值小於 50%) 或陰性 (LVEF 值大於 50%)，代表檢查結果一致；否則定義為不一致。以此方法區別出兩種核醫檢查做法，何者之診斷結果與心臟超音波相關性較高。

結果與討論

心臟疾病高居國人十大死因的第二位，其中急性心肌梗塞是最常見的急重症之一 [3]，經由心室壁運動之評估可偵測慢性動脈疾病之病變情形，如有運動不能或運動障礙則必須考慮有室壁瘤的可能；有運動機能減退則可能為心肌缺血或疤痕。對急性心肌梗塞病人而言，LVEF 可為癒後的指標。研究顯示，在急性心肌梗塞發生後 24 小時內，若 LVEF $< 30\%$ ，則約有 55% 的病人會於住院中死亡；若 LVEF $> 30\%$ ，住院中之死亡率則只有 2%。對於長期性的癒後，LVEF 亦是一項良好的指標。若 LVEF $< 40\%$ 以下，則急性心肌梗塞發生一年後，其死亡率會相對增加；當 LVEF $< 30\%$ 以下時，死亡率增加之比例則更明顯。

心臟超音波由於其安全性、易用性和對心臟結構功能全面評估的能力，是評估心臟衰竭 (HF) 患者最廣泛使用的工具 [4]。3D 心臟超音波推出後，比起傳統超音波有著較佳的可信度 (reliability) 和較低的變異性 (variability)，所以傳統的方法或許可被 3D 心臟超音波取代 [5]。

在本研究中總共有 66 名病人 (其中一名病人執行平面造影和斷層造影兩種檢查)，54 名為男性，佔總人數 82%；12 名為女性，佔總人數 18%。男性年齡平均數為 67.6 歲，中位數為 67 歲，年齡範圍 37-98 歲。女性年齡平均數為 70 歲，中位數為 69 歲，年齡範圍 65-93 歲 (表 1)。資料顯示，總人口的心臟衰竭盛行率為 2.0-3.9%，

表 1. 病人資料表

性別	人數 (位)	百分比 (%)	年齡 平均數 (歲)	年齡 中位數 (歲)	年齡範圍 (歲)
男	54	72	67.6	67	37-98
女	12	18	70	69	65-93

且男女性別比為 1:1。在所有年齡族群中，女性的盛行率都較男性來得低，但此差異會隨著年齡增加而變小。這也表示隨著女性族群若比男性族群年長，她們 (75 歲以上女性) 的心臟衰竭發生率也會變得比較高 [6]。

關於 LVEF，大量研究描述了平面與斷層造影之間的良好相關性 [1]。Daou 等人將 LVEF 的平面造影和 LV 容積的數位放射血管造影作為黃金標準，證明造影對於 LVEF 和體積測量具有高度可重複性、簡單和準確。Van Krieking 等人比較斷層與平面造影之 LVEF，結果為高度相關 ($r = 0.89$, $P < 0.004$)，且 Bland-Altman 分析顯示平面造影的平均差異高出 3.3% ($P = 0.0072$) [7]。

LVEF 平均值

對於使用斷層造影計算 LVEF，所有患者均成功利用 QBS 自動圈畫 ROI。斷層造影與心臟超音波、平面造影與心臟超音波測量出的平均 LVEF 值分別是 $45.2 \pm 21.43\%$ 與 47.19 ± 14.45 ， $43.20 \pm 13.64\%$ 與 47.66 ± 13.71 (表 2)。

皮爾森積差相關分析 (Pearson Correlation)

比較平面造影、斷層造影和心臟超音波的 LVEF 值，並以心臟超音波之 LVEF 作為參考標準。

從平面造影得出的 LVEF 值亦顯示出與心臟超音波有相關性 ($r = 0.772$; $P = 0.000$)。從斷層造影得出的 LVEF 值顯示出與心臟超音波有相關性 ($r = 0.729$; $P = 0.000$) (表 2)。

因此無論是平面造影或斷層造影，其檢查結果皆與心臟超音波之 LVEF 值有相關性。表示若以相關性分析，兩種檢查結果與心臟超音波之一致性相當高。

檢查結果之一致性

進行平面造影與心臟超音波檢查總共 33 例，其中 27 例兩者檢查結果一致，結果一致性為 82% (表 3)。進

行斷層造影與心臟超音波檢查總共 34 例，其中 24 例兩者檢查結果一致，一致性為 71% (表 3)。根據此結果了解平面與斷層造影兩者之檢查結果，皆與心臟超音波檢查結果相近。

平面與斷層造影在收取及處理影像之差異

平面造影在收取影像時以 LAO 45 度為首選 (Septal wall 較好看)，但對於不同病人，能將心房心室分開的角度未必都是 45 度，因此經常需要微調角度，可能增加人為干擾之影響。另外，平面造影為避免腔室受到不同角度的限制，所以要評估心壁運動至少需要收取三個不同角度的影像 (分別是 Anterior、lateral、LAO view)，若收取三個角度所需時間，則與斷層造影收取影像時間相近，且斷層造影可透過斷層掃描來區分左心室和右心室，而平面造影無法，因此斷層造影提供的資訊更多。

斷層造影在影像處理中，能提供容積評估 (Volumetric assessment) 的資訊，如：End-systolic volume

、End-diastolic volume 等；而平面造影只看計數的變化。除此之外，斷層造影使用 QBS 軟體處理影像，此軟體多為自動處理，不需個別圈畫 End-systolic 和 End-diastolic 的 ROI，可以減少人為誤差。

限制

QBS 軟體用於斷層造影自動處理，因為使用全心處理，所以只要 RV 和 LV 界限夠清楚，則不需要操作人員干預。但若界線不清楚，RV 和 LV 則需手動調整。

此研究並未排除心律不整病人。另外，若在肺動脈高壓的情況下，很難清楚地定義心中膈和界定左心室位置 [7]。

這些資料皆是以超音波結果作為比較對象，但是超音波之檢查結果容易受到操作者影響甚深，再現性不佳，故本篇資料以呈現平面與斷層影像結果和超音波之間的關係為主。

表 2. 核醫造影與心臟超音波之 LVEF 及相關性

	平面造影組		斷層造影組	
	平面造影	心臟超音波	斷層造影	心臟超音波
LVEF (mean ± sd)	43.20 ± 13.64	47.66 ± 13.71	45.24 ± 21.43	47.19 ± 14.45
兩者相關係數	0.772		0.729	
兩者顯著性 (P 值)	0.000		0.000	

表 3. 核醫造影與心臟超音波之一致性

	平面造影組		斷層造影組	
	平面造影	心臟超音波	斷層造影	心臟超音波
LVEF > 50% 之人數	7	14	14	14
LVEF < 50% 之人數	26	19	20	20
總人數	33		34	
結果一致人數	27		24	
兩者一致性	0.82		0.71	

結 論

在本研究中，以心臟超音波當成參考標準，利用皮爾森積差相關分析了解平面造影、斷層造影和心臟超音波之相關性，發現兩種核醫檢查皆與心臟超音波具有相關性。

在檢查結果一致性中，將平面造影與心臟超音波，以及斷層造影與心臟超音波分成兩組資料，並比較各自的LVEF值，兩者之檢查結果，皆與心臟超音波檢查結果相近。

綜合研究結果與參考文獻，平面與斷層造影皆為良好之檢查工具，兩者之檢查結果與檢查時間相當。但斷層造影可以提供較多的臨床資訊且受人為干擾影響較少，因此目前臨床已常規使用斷層造影作為評估心室功能之檢查方式。

參考文獻

1. 林昆儒、蔡名峰·核醫心室功能檢查 Multigated Blood Pool Analysis (MUGA) 2014。Available from: <https://kelwww.cgmh-mi.com/examm/muga>. Accessed: 2021/09/01
2. Marcus Hacker XH, Sandra Kupzyk et al. Clinical validation of the gated blood pool SPECT QBS processing software in congestive heart failure patients: correlation with MUGA, first-pass RNV and 2D-echocardiography. *The International Journal of Cardiovascular Imaging*. 2006;22.
3. 賴苑惠、蘇界守、王國陽·急性心肌梗塞臨床成效指標之監測與應用—以台中榮總心臟血管中心為例·*醫療品質雜誌*, 2013;7(4): 39-42.
4. Alaa Mabrouk Salem Omar MB, Partho P. Sengupta. Advances in Echocardiographic Imaging in Heart Failure With Reduced and Preserved Ejection Fraction. *Circulation Research*. 2016;119:357-74.
5. 王宗道 林·如何診斷正常收縮功能之心臟衰竭：超音波及核磁共振所扮演的角色 2010。Available from: <https://www.tsoc.org.tw/upload/journal/2/20100701/2.pdf>.
6. K. S-G. 心臟衰竭之性別差異 2012。Available from: <https://gms.kmu.edu.tw/?p=270>. Accessed:2021/09/06
7. Hugo Lavados J. CR, Héctor Gatica. Comparison of radionuclide ventriculography using SPECT and planar techniques in different cardiac conditions. *Eur J Nucl Med Mol Imaging*. 2007;34.

The Radionuclide Ventriculography Using Planar and SPECT (Single Photon Emission Tomography) Techniques to Explore the Correlation with Echocardiography

Tzu-Chi Chang^{1,2}, Shih-Chin Chou¹, Yu-Sheng Hung^{1*}

¹Division of Nuclear Medicine, Chi Mei Medical Center, Liouying, Tainan, Taiwan

²Department of Medical Imaging and Radiological Sciences, Kaohsiung Medical University

Abstract

Purpose: The aim of this study was to understand which of SPECT image and planar image has a higher correlation with cardiac ultrasound results, and to use cardiac ultrasound as a reference standard for LVEF.

Materials and Methods: Between 2015/08/10-2020/01/09, patients for heart function assessment with planar study and/or SPECT and cardiac ultrasound. LVEF defined by each study were recorded. In vivo Tc-99m labeled RBC method was used. Images were taken by gamma camera, and then LVEF was calculated by e-soft software and QBS algorithm. The definition of positive is less than 50% of LVEF. Then data was analyzed by SPSS 18 and excel.

Results: 54 men and 12 women were included. The average LVEF values measured by SPECT image and cardiac ultrasound, planar image and cardiac ultrasound were $45.2 \pm 21.43\%$ and 47.19 ± 14.45 , $43.20 \pm 13.64\%$ and 47.66 ± 13.71 , respectively. There showed significantly high correlation between LVEF measured by SPECT image and cardiac ultrasound ($r = 0.729$, $p < 0.001$) and LVEF measured by planar image and cardiac ultrasound ($r = 0.772$, $p < 0.001$). The results of both planar and SPECT image are similar to those of cardiac ultrasound.

Conclusion: SPECT can provide more clinical information and is less affected by human interference. SPECT has been routinely used clinically as an examination method to assess ventricular function.

Key words: echocardiography, MUGA, Planar image, SPECT image

J Nucl Med Tech 2022;19:1-7

Received 2022/4/28

Corresponding author: Yu-Sheng Hung

Division of Nuclear Medicine, Department of Medical Image, Chi Mei Medical Center, Liouying

Address: No. 201, Taikang, Liouying Dist., Tainan 736, Taiwan, R.O.C.

Tel: 06-6226999 ext. 71042; E-mail: clh5800@mail.chimei.org.tw

Geiger-Müller Counter Kit Basic Test: Counting Statistics and Fluorine-18 Decay Curve Counting

Fa-Shun Tsai*, Tai-Lin Jiang, Lin-Chun Ou, Cheng-Hui Lee

Division of PET Center, Shin Kong Wu Ho-Su Memorial Hospital, Taipei, Taiwan

Abstract

Geiger-Müller counter, often known as a Geiger counter or Geiger tube, is a type of ionizing radiation detector. Because of their simple structure, low cost, and ease of use, Geiger counters are widely employed in nuclear physics, medicine, and industry. A Geiger-Müller counter DIY kit was used in this experiment to conduct counting statistics and half-life counting tests to evaluate the counter kit's counting performance.

Materials and methods: The Geiger-Müller counter kit (CAJOE, Model: GC-1602-NANO) and Geiger tube model J305βγ are used in this experiment. The arduino nano circuit board is connected to the computer for the experiment. The software code is written and uploaded with the arduino IDE. We use the Tera Term port monitoring software to record the counts returned by the arduino nano board. Set the Geiger-Müller counter to 25 cm from the ^{137}Cs radioactive source and record the counting value 390 times for 60 seconds each time (counts per minute, CPM). Half-life test: Place the 17 μCi ^{18}F -FDG at a distance of 3 cm from the Geiger-Müller counter and record the counting value 500 times for 60 seconds each time. The half-life was calculated by curve fitting.

Results: Counting statistics test results, the average count rate at 25 cm from the ^{137}Cs radioactive source is 739.92 ± 26.29 CPM, and the histogram shows a Gaussian distribution. The half-life test results show that the measured count rate curve is an exponential decay curve. The curve fitting equation is $y = 4997e^{-0.00614x}$. According to the half-life curve equation, the calculated half-life is 112.89 minutes, which is very close to the ^{18}F -FDG physical half-life of 109 minutes.

Conclusion: The results of this experimental test confirm that this Geiger-Müller counter kit can perform basic free radiation detection and can be used for teaching or applications related to radiology or radiation protection.

Key words: Geiger-Müller counter, Geiger tube, counting statistics, Gaussian distribution, half-life

J Nucl Med Tech 2022;19:9-15

Ionizing radiation is a type of energy released by atoms in the form of electromagnetic waves or particles that have sufficient energy to ionize atoms or molecules by detaching electrons from them. People are exposed to natural sources of ionizing radiation, such as in soil, water, and vegetation, as well as in human-made sources, such as x-rays and medical devices [1, 2]. However, this radiation is not easily detected and since it also possesses high ionizing power and penetration strength, it constitutes a risk to human

Received 2022/5/25

Corresponding author: Fa-Shun Tsai

Division of PET Center, Shin Kong Wu Ho-Su Memorial Hospital, Taipei, Taiwan

Address: No. 95, Wenchang Rd., Shilin Dist., Taipei City 111, Taiwan (R.O.C.)

Division of PET Center

E-mail: T005629@ms.skh.org.tw

health when it is found outside of its acceptable limits [3]. Because humans cannot see or feel ionizing radiation, we need radiation-sensitive detectors to detect it. Geiger-Müller counter (GM counter) often known as a Geiger counter or Geiger tube, is a type of ionizing radiation detector. Because of their simple structure, low cost, and ease of use, Geiger counters are widely employed in nuclear physics, medicine, and industry [3, 4]. Geiger-Müller counter is named after Hans Geiger, a German scientist, who worked on detecting radiation in the early 1900s. Walter Mueller, a graduate PhD student of Geiger's, perfected the gas-sealed detector in the late 1920s and received credit for his work when he gave his name to the Geiger-Mueller tube (GM tube) [5].

A Geiger-Müller counter is a gas-filled detector consisting of a gas-filled tube connected to a high-voltage circuit that utilizes the ionization of gas by radiation as the primary tool for detecting radiation. A typical GM tube is a chamber filled with mixture gas. The chamber has two electrodes with a potential differential of several hundred volts between them. The cathode is a wire positioned axially in the middle of the chamber, whereas the anode is a metal tube with its interior surface coated with a conducting substance or a spiral wire. Ionization of the noble gas occurs when radiation strikes the tube window. The expelled electrons will be drawn to the anode, while the heavier ions will be drawn to the cathode. The current causes the voltage between the anode and cathode to drop which the counter detects as a signal [3-5].

Now we can easily buy commercial Geiger counters or DIY kits on the Internet. DIY project information on Geiger counters is also easy to find online. In this experiment, a Geiger-Müller counter kit was used for counting statistics and half-life counting tests to evaluate the counting performance of this counter kit.

Materials and methods

The Geiger-Müller counter kit (CAJOE, Model: GC-1602-NANO) and Geiger tube model J305 $\beta\gamma$ are used in this experiment. The arduino nano circuit board is connected to the computer for the experiment. Figure 1 depicts the entire



Figure 1. The Geiger-Müller counter kit (CAJOE, Model: GC-1602-NANO) is equipped with a J305 $\beta\gamma$ Geiger tube and an arduino nano circuit board. This experiment did not use the LCD screen shown in the figure.

experimental GM counter kit. The software code is written and uploaded with the arduino IDE. The user interface of the arduino IDE and the basic code of this experiment are shown in Figure 2. We use the Tera Term port monitoring software to record the counts returned by the arduino nano board.

Counting statistics test: We use a cesium-137 (Isotope Product Laboratories, Model: CA818-843-7000) as the standard radioactive source. The half-life of cesium 137 is 30.05 years, which is much longer than the experimental period, and the activity can be regarded as a constant during this experiment. Set the Geiger-Müller counter to 25 cm from the ^{137}Cs source and record the counting value 390 times for 60 seconds each time. Half-life test: Place the 17 μCi ^{18}F -FDG at a distance of 3 cm from the Geiger-Müller counter and record the counting value 500 times for 60 seconds each time. The half-life was calculated by the curve fitting equation.

We measured the working voltage of the Geiger tube according to the manufacturer's documentation before starting the experiment. According to the document of J305 $\beta\gamma$ type Geiger tube, the recommended working voltage is 380 volts, and the actual measured value is 390.4 volts. We must subtract the background value from the measurement


```

Geiger_Counter_CPM | Arduino 1.8.19
檔案 編輯 草碼碼 工具 說明

Geiger_Counter_CPM
// Counts per minute

unsigned long counts;           //設定變數counts
unsigned long previousMillis;   //設定變數previousMillis
void impulse() {               // impulse() 函式定義為counts變數自加
  counts++;
}

#define LOG_PERIOD 60000       // 每60秒紀錄一次
void setup() {                //設定
  counts = 0;                 //初始化counts = 0
  Serial.begin(9600);         //Serial.begin (Baud Rate): Baud Rate指從一裝置發到另一裝置的位元率, 即 (bit/s)
  pinMode(2, INPUT);         //引腳 2為INPUT
  attachInterrupt(digitalPinToInterrupt(2), impulse, FALLING); // 每次引腳 2 上有FALLING信號時調用impulse函式
  Serial.println("Start Counting"); // 端口列印"Start Counting"
}

void loop() {                 //主迴圈
  unsigned long currentMillis = millis(); //millis() 函式會回傳Arduino 從開始執行程式 一直到目前為止的千分之一秒數值 (number of milliseconds)
  if (currentMillis - previousMillis > LOG_PERIOD) { //每當currentMillis - previousMillis > 60
    previousMillis = currentMillis; //更新 previousMillis數值
    Serial.println(counts); // 端口列印一次counts變數數值
    counts = 0; //counts變數數值重新歸0
  }
}
    
```

Figure 2. The user interface of the arduino IDE and the basic code of this experiment.

for experimental accuracy. Turn on the GM counter for 10 minutes and then record the background counting value 100 times for 60 sec each time, the unit is counts per minute (CPM), and the average value is taken as the background counting value. The background counting value is 20.3 CPM. All measurements in this experiment will be converted to counts per minute (CPM).

Results

The results of the counting statistics experiment are shown in Figure 3. A total of 390 counting tests were recorded, with an average counts and standard deviation of 739.92 ± 26.29 CPM. The probability distribution diagram (histogram) and Gaussian fitting curve of the experimental results of counting statistics are shown in Figure 4. The histogram basically presents a normally distributed bell shape that is symmetrical on both sides.

^{18}F -FDG half-life count curve and exponential decay fitting curve are shown in Figure 5. The half-life of fluorine-18 is 109.771 minutes. Half-life test exponential decay fitting curve equation: $y = 4997e^{-0.00614x}$. An exponential decay curve fits the following equation: $N(t) = N_0 e^{-\lambda t}$. The half-life $t_{1/2}$ of the decay is related to the decay constants λ in the following way: $t_{1/2} = \ln 2 / \lambda$. According to the exponential

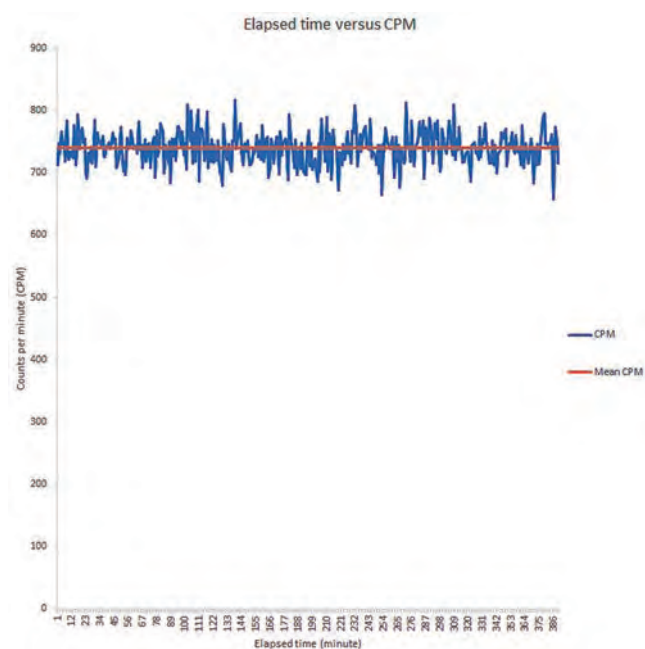


Figure 3. Elapsed time versus CPM.

decay fitting equation, the half-life should be 112.89 minutes, which is 102.84% of the true value.

Discussion

Radioactive decay is a random process [6]. We can't predict exactly when an unstable nucleus will decay; all we

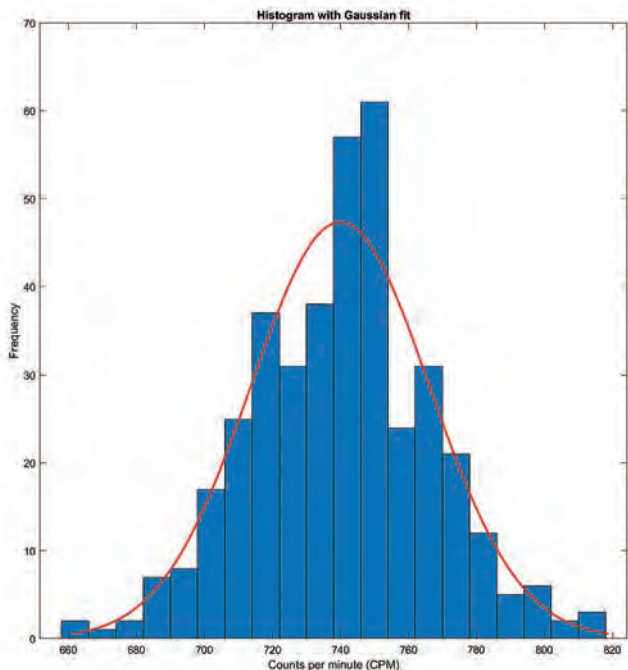


Figure 4. Histogram of counting value and Gaussian fit curve.

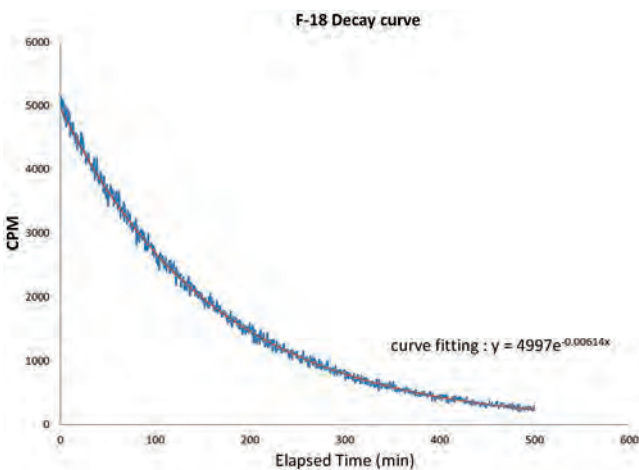


Figure 5. ^{18}F -FDG half-life counting curve and Exponential decay curve fitting.

can do is predict the probability that it will decay within a given time frame. Similarly, we can only anticipate the average number of decays in a radioactive sample during a given time interval, rather than the precise number of decays. We receive a varied number of counts each time we count the number of decays in a fixed time interval, but they have a more or less clear mean value. Therefore, even if the exact

same experimental conditions are kept, for example, the time of each measurement in the experiment remains the same, the half-life of the radioactive source is very long, the position of the radioactive source relative to the counter is kept constant, etc., in the radioactivity measurement, each time The results of the experimental measurements are different. The results of each experimental measurement are not identical, but rather fluctuate around an average value, with large differences in some measurements. This phenomenon is known as radioactivity count statistics [6-9]. This radioactivity count statistic reflects the inherent properties of radioactive nuclear decay, regardless of the measuring instruments and techniques used. The experimental results in Figure 1, which shows that the experimental results fluctuate around the mean CPM value.

The statistical distribution of the decay of radioactive nuclei can be deduced according to the theory of mathematical statistical distribution. The decay process of radioactive nuclei is a process that is independent of each other, that is, the decay of each nucleus is completely independent, and which nucleus decays first and which nucleus decays later is purely accidental, and there is no certain order. There are only two states of an atom per unit time in a radioactive source: decay or no decay. Assume the decay probability is $p = (1 - e^{-\lambda t})$, and the probability of no decay is $q = e^{-\lambda t}$, where λ is the decay constant. The half-life $t_{1/2}$ can be expressed as $\ln 2 / \lambda$. Assuming that at time $t = 0$, the total number of radioactive nuclei is N_0 , some of the nuclei n will decay at time t . According to the binomial distribution, the probability $p(n)$ of the decay of n nuclei in time t can be obtained as:

$$p(n) = \frac{N_0!}{(N_0-n)!n!} p^n (1-p)^{N_0-n}$$

$$= \frac{N_0!}{(N_0-n)!n!} (1 - e^{-\lambda t})^n (e^{-\lambda t})^{N_0-n} \quad (1)$$

In time t , the average number of decayed particles is m , $m = N_0 p = N_0 (1 - e^{-\lambda t})$. The root-mean-square deviation (standard deviation) is σ :

$$\sigma = \sqrt{N_0 p q} = \sqrt{m(1-p)} = \sqrt{m e^{-\lambda t}} \quad (2)$$

If $\lambda t \ll 1$ or $t \ll 1/\lambda$, the time t is much smaller than the half-life $\ln 2/\lambda$, at this point, the probability of no decay q approaches 1. And the root-mean-square deviation σ can be simplified as:

$$\sigma = \sqrt{m} \quad (3)$$

In the decay process, when N_0 is large and λt is much less than 1 ($\lambda t \ll 1$), the binomial distribution equation (1) can be simplified as follow:

$$\begin{aligned} \frac{N_0!}{(N_0-n)!n!} &\approx N_0^n \text{ and } (1-p)^{N_0-n} \\ &\approx (e^{-p})^{N_0-n} = e^{-pN_0} \end{aligned} \quad (4)$$

The binomial distribution equation (1) can be simplified as Poisson distribution equation as:

$$p(n) = \frac{N_0^n}{n!} p^n e^{-pN_0} = \frac{m^n}{n!} e^{-m} \quad (5)$$

In the Poisson distribution, the value range of n is all positive integers (0, 1, 2, 3, ...), and when $n = m$, $p(n)$ has a maximum value. In a Poisson distribution, the expectation value $E(x) = m$ and $\sigma^2 = m$. When m is small, the distribution is asymmetric; when m is larger, the distribution asymptotically approaches symmetry, and the Poisson distribution can generally be replaced by a normal (Gaussian) distribution [6, 7, 9]. In mathematics, Stirling's approximation or Stirling's formula is an approximation for n factorials.

$$\text{Stirling's formula: } n! \approx \sqrt{2\pi n} \left(\frac{n}{e}\right)^n \quad (6)$$

Then the equation (5) can be modified as follow:

$$p(n) = \frac{m^n}{n!} e^{-m} = \frac{1}{\sqrt{2\pi\sigma}} e^{-\frac{(n-m)^2}{2\sigma^2}} \quad (7)$$

Poisson distribution is very well approximated by the Gaussian or normal distribution [6, 7, 9]. For which certain confidence intervals have been established in terms of the standard deviation. These confidence intervals (CI) are as follows: About 68% of values drawn from a normal distribution are within one standard deviation σ away from the mean; about 95% of the values lie within two standard deviations; and about 99.7% are within three standard deviations [10]. We sorted the ^{137}Cs counting results according to the confidence levels as shown in Table 1.

The nuclear decay process follows: $N(t) = N_0 e^{-\lambda t}$. Among them, N is the number of atoms that have not decayed, and N_0 is the number of atoms at the initial time $t = 0$, which means that N decreases with the increase of time t , which is a process that satisfies exponential decay. Each radioisotope has a different physical half-life, and a half-life counting test can be used to determine isotope purity. The results of the ^{18}F half-life counting experiment demonstrate this exponential decay process. The output of a usable ionizing radiation meter should be positively correlated with the intensity of the detected radiation. The results of this experiment confirm that the value of the Geiger counter is proportional to the intensity of the radiation.

Conclusion

The results of this experiment confirmed that the Geiger counter can detect ionizing radiation and that the counting value is proportional to the radiation intensity. The results of this experiment confirm that this Geiger-Miller counter kit can detect basic ionizing radiation and can be used to teach radiology or radiation protection.

Table 1. ^{137}Cs counting results and confidence interval analysis

CI	CPM range	Samples within CI	Percentage	Theoretical percentage
Mean+1 σ	713.62~766.22	270	69.23%	68%
Mean+2 σ	687.33~792.51	369	94.62%	95%
Mean+3 σ	661.03~818.81	389	99.74%	99.7%

References

1. Organization, W. H. *Ionizing radiation, health effects and protective measures*. 2016 [cited 2016 29 April]; Available from: <https://www.who.int/news-room/fact-sheets/detail/ionizing-radiation-health-effects-and-protective-measures>.
2. Wikipedia, c., Ionizing radiation, in Wikipedia, The Free Encyclopedia.
3. Silva, M. D. R., *Ionizing radiation detectors*. Evolution of Ionizing Radiation Research, 2015: p. 189-209.
4. Hinch, W. H. and U. S. A. E. Commission, *Geiger Counter Radiation Meter*. 1947: U.S. Atomic Energy Commission.
5. Geiger, H. and W. Müller, *Elektronenzählrohr zur messung schwächster aktivitäten*. Naturwissenschaften, 1928. 16(31): p. 617-618.
6. L'Annunziata, M. F., *Handbook of Radioactivity Analysis*. 2003: Elsevier Science.
7. Knoll, G. F., *Radiation Detection and Measurement*. 2000: Wiley.
8. Leo, W. R., *Techniques for Nuclear and Particle Physics Experiments: A How-To Approach*. 1994: Springer Berlin Heidelberg.
9. Tsoulfanidis, N. and S. Landsberger, *Measurement and Detection of Radiation*. 2021: CRC Press.
10. Wikipedia, c., Normal distribution, in Wikipedia, The Free Encyclopedia.

蓋格米勒計數器套件基本測試： 計數統計與氟-18 衰減曲線計數

柴發順* 江泰林 歐玲君 李正輝

新光吳火獅紀念醫院 正子造影中心

中文摘要

前言：蓋格米勒計數器也稱為蓋格計數器或蓋格管，是一種用於偵測游離輻射的輻射偵測器。蓋格計數器因為結構簡單、造價低廉、使用方便，被廣泛使用於核子物理、醫學及工業等領域中。本次實驗以一台蓋格米勒計數器套件進行計數統計與半衰期計數測試，評估此計數器套件的計數性能。

材料與方法：本實驗採用蓋格米勒計數器套件 (CAJOE, Model: GC-1602-NANO)，蓋格管型號 J305βγ，以 arduino nano 電路板連接電腦進行實驗，軟體程式以 arduino IDE 編寫上傳後利用 Tera Term 端口監視軟體紀錄 arduino nano 電路板傳回的計數值。計數統計測試：¹³⁷Cs 放射源 (Model: CA818-843-7000)，實驗當日活性 128.5 μCi。將蓋格米勒計數器套件成品固定在 ¹³⁷Cs 放射源 25 公分處，以 USB 連接紀錄計數值，連續紀錄 390 次，每次計數 60 秒 (每分鐘計數值，CPM)。半衰期測試：將放射活性 17 μCi 的 ¹⁸F-FDG 固定在蓋格米勒計數器 3 公分處，紀錄 500 次，每次 60 秒。以曲線擬合推算半衰期。

結果：計數統計測試結果，¹³⁷Cs 放射源 25 公分處計數率平均值為 739.92 ± 26.29 CPM，直方圖呈高斯曲線分布。半衰期測試結果，測量計數率曲線呈指數衰減曲線，擬合曲線 $y = 4997e^{-0.00614x}$ ，依照半衰期曲線公式換算半衰期 $t_{1/2} = 112.89$ 分鐘與 ¹⁸F-FDG 物理半衰期 109 分鐘極為接近。

結論：本實驗測試結果證實此型蓋格米勒計數器套件可進行基本游離輻射偵測，可應用於放射線學或輻射防護相關教學。

關鍵詞：蓋格米勒計數器、蓋格管、計數統計、高斯分布、半衰期

核醫技學誌 2022;19:9-15

接受日期：2022 年 5 月 25 日

通訊作者：柴發順

聯絡地址：台北市士林區文昌路 95 號 新光吳火獅紀念醫院正子造影中心

電子郵件：T005629@ms.skh.org.tw

Evaluation of Radiation Shielding Ability of Different Materials Anti-epidemic Partitions: Monte Carlo Experiment

Fa-Shun Tsai*, Tai-Lin Jiang, Lin-Chun Ou, Cheng-Hui Lee

Division of PET Center, Shin Kong Wu Ho-Su Memorial Hospital, Taipei, Taiwan

Abstract

Introduction: Droplet transmission has been identified as the primary route of SARS-CoV-2 transmission since the outbreak. SARS-CoV-2 infection primarily causes respiratory illness, ranging from mild to severe illness and death. Many studies have also shown that wearing personal protective masks, protective clothing, and using partitions can prevent droplet transmission and thus SARS-CoV-2 transmission. The partition board is also widely used in the hospital's ionizing radiation departments, such as the radiology and nuclear medicine departments. Staffs working in the ionizing radiation department have a high chance of being exposed to radiation. Partition partitions of different materials can provide protection against droplet infection, but the shielding effect of radiation photons is not clear. In this experiment, Monte Carlo simulation software is used to simulate several partition materials to evaluate the shielding effect of each material on radiation photons.

Materials and Methods: GATE software was used to simulate 140 kVp X-ray and 140 keV, 511 keV single-energy γ photons irradiating a 30×30×30 cm water phantom. Simulate the dose distribution of direct beam irradiation and irradiation with partition shielding, respectively. Simulation of 10^6 photons per exposure.

Partition materials include 2 mm thick stainless steel (SS304), 2 mm aluminum, 5 mm glass, 5 mm acrylic (PMMA). Record the radiation dose (Gray) per millimeter in the water phantom.

Result: In the 140 kVp X-ray simulations using 2 mm thickness stainless steel, 2 mm aluminum, 5 mm glass and 5 mm acrylic partitions, the absorbed dose was 28.19%, 86.39%, 75.63% and 91.93% of the direct irradiation respectively. The simulated results for 140 keV mono-energy γ photon irradiation was 76.75%, 94.78%, 88.12% and 93.95% of the direct irradiation respectively. And 511 keV mono-energy γ photon irradiation simulations were 91.2%, 96.89%, 92.78% and 96.19% of the direct irradiation.

Conclusion: The results of this simulation show that 2 mm SS304 stainless steel has a better radiation shielding efficiency against X-rays reducing the radiation dose by approximately 70%. All other materials failed to achieve the desired radiation shielding effect at all photon energies. Among of the transparent materials, glass provide better shielding than acrylic at all photon energies. Metal and plastic partitions do not offer adequate shielding efficiency at 511 keV photon irradiation. To avoid unnecessary radiation exposure, nuclear medicine staffs should be aware that anti-epidemic partitions do not provide significant radiation protection.

Key words: Monte Carlo simulation, radiation shielding, anti-epidemic partition, GATE, Geant4

J Nucl Med Tech 2022;19:17-24

Received 2022/9/15

Corresponding author: Fa-Shun Tsai

Division of PET Center, Shin Kong Wu Ho-Su Memorial Hospital, Taipei, Taiwan

Address: No. 95, Wenchang Rd., Shilin Dist., Taipei City 111, Taiwan (R.O.C.)

Division of PET Center

E-mail: T005629@ms.skh.org.tw

Introduction

Droplet transmission has been identified as the primary route of SARS-CoV-2 transmission since the outbreak. Contact, droplet, airborne, pollutant, fecal-oral, blood-borne, mother-to-child, and animal-to-human transmission are all possible modes of SARS-CoV-2 transmission [1]. SARS-CoV-2 infection primarily causes respiratory illness, ranging from mild to severe illness and death. Many studies have also shown that wearing personal protective masks, protective clothing, and using partitions can prevent droplet transmission and thus SARS-CoV-2 transmission. The partition grid is also widely used in the hospital's ionizing radiation inspection departments, such as the radiology and nuclear medicine departments [2-5]. Staffs working in the ionizing radiation department have a high chance of being exposed to radiation [6-9]. In order to protect workers from ionizing radiation, these departments are equipped with a lot of shielding devices such as caps, lead glasses, thyroid protectors, aprons, radiation reducing gloves, and so on [10]. Anti-epidemic partitions of different materials can provide protection against droplet infection, but the shielding effect of radiation photons is not clear. In this experiment, Monte Carlo simulation software is used to simulate several common separator materials to evaluate the shielding effect of each material on radiation photons.

Materials and Methods

The GEANT4 Application for Emission Tomography (GATE) encapsulates the GEANT4 libraries in order to achieve a modular, versatile, scripted simulation toolkit adapted to the field of nuclear medicine. In particular, GATE provides the capability for modeling time-dependent phenomena such as detector movements or source decay kinetics, thus allowing the simulation of time curves under realistic acquisition condition. GATE in particular offers the capacity to simulate time curves under realistic acquisition conditions by simulating time-dependent phenomena like detector motions or source decay kinetics [11, 12]. It can also be used for dose calculation in radiation therapy, brachytherapy or any other application [13]. All of the Monte

Carlo simulations were performed using the GATE version 9.1 with GEANT4 version 10.7.0 in this study. GATE software was used to simulate 140 kVp X-ray and 140 keV, 511 keV single-energy γ photons irradiating a 30×30×30 cm water phantom. Simulate the dose distribution of direct beam irradiation and irradiation with partition shielding, respectively. Simulation of 106 photons per exposure. Partition materials include 2 mm thick stainless steel (SS304), 2 mm aluminum, 5 mm glass, 5 mm acrylic (poly methyl methacrylate, PMMA). The primary method for defining the properties of the materials used in Gate is by a materials database (built-in GateMaterials.db file). This GateMaterials.db file holds all the information required for Gate to assign the nuclear properties from the Geant4 data sets. The materials for this experiment were set in the GateMaterials.db file as shown in Figure 1. In Gate, materials are defined as combinations of elements. In the case of 304-stainless steel, the various mass fractions are given as 0.695 Iron, 0.190 Chromium, 0.095 Nickel, and 0.020 Manganese. Note that the mass fractions from the elements must all sum to one.

GATE allows to simulate the dose distribution in a phantom during radiotherapy. The Dose measurement (DoseActor) is the tool that is used to store the deposited dose. We record the radiation dose (Gray, Gy) per millimeter in the water phantom. The 140 kVp X-ray spectrum is

```
[Materials]
SS304: d=7.92 g/cm3 ; n=4 ; state=solid
      +el: name=Iron      ; f=0.695
      +el: name=Chromium ; f=0.190
      +el: name=Nickel   ; f=0.095
      +el: name=Manganese ; f=0.020

Aluminium: d=2.69890 g/cm3 ; n=1 ; state=solid
          +el: name=auto    ; n=1

Glass: d=2.5 g/cm3; n=4; state=solid
      +el: name=Sodium     ; f=0.1020
      +el: name=Calcium   ; f=0.0510
      +el: name=Silicon   ; f=0.2480
      +el: name=Oxygen    ; f=0.5990

PMMA: d=1.19 g/cm3 ; n=3 ; state=solid
      +el: name=Hydrogen  ; f=0.080538
      +el: name=Carbon   ; f=0.599848
      +el: name=Oxygen   ; f=0.319614
```

Figure 1. The materials for this experiment were set in the GateMaterials.db file.

generated by SPEKTR 3.0. The SPEKTR is a computational toolkit which has been developed to calculate X-ray spectra based on the TASMICS algorithm, updating previous work based on the TASMIP spectral model [14, 15]. The toolkit includes a Matlab function library and improved user interface (UI) along with an optimization algorithm to match calculated beam quality with measurements.

System geometric setting: The Photon source set as a point source, GATE code defines as “General Particle Source”. Photon beam is directed towards the water phantom, the beam modeling as a narrow cone beam with 1 degree span. Photon source to water phantom surface distance (Source surface distance, SSD) is 55 cm. The partition plate is set between the photon source and the water phantom, 25 cm away from the surface of the water phantom. The system geometry settings are shown in Figure 2.

Result

We have sorted out the radiation dose results of each simulated exposure to the water phantom and listed them in Table 1. Assuming that the absorbed dose directly irradiated by photons of different energy is 100%, the absorbed dose

percentage after shielding with different material separators is shown in Table 2. The X-ray spectrum incents the water cube with and without partition materials shielding were showed

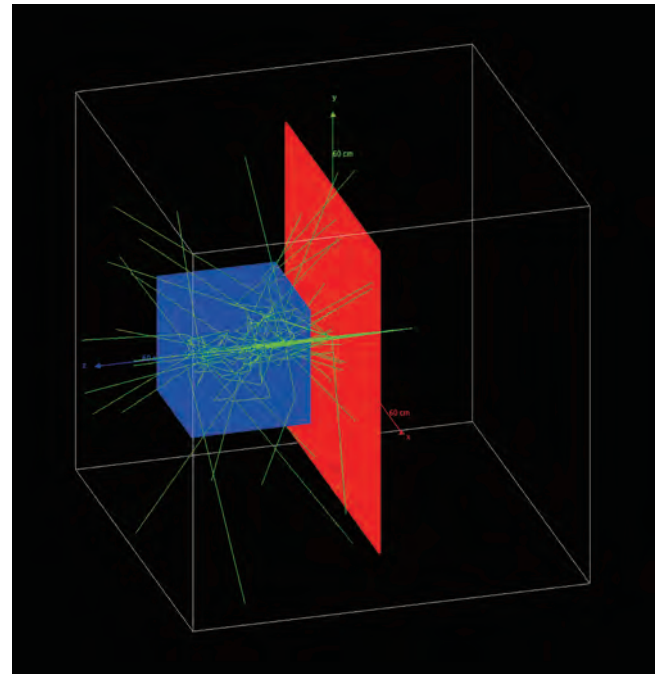


Figure 2. System geometry setting 3D display with photon trajectories.

Table 1. Absorbed dose within the water phantom of each simulation

	Total absorbed dose within the water phantom (Gy)				
	No partition	2 mm SS304	2 mm Al	5 mm Glass	5 mm PMMA
140 kVp X-ray	7.36×10^{-8}	2.07×10^{-8}	6.36×10^{-8}	5.56×10^{-8}	6.76×10^{-8}
140 keV γ -ray	1.43×10^{-7}	1.10×10^{-7}	1.36×10^{-7}	1.26×10^{-7}	1.34×10^{-7}
511 keV γ -ray	5.79×10^{-7}	5.28×10^{-7}	5.60×10^{-7}	5.37×10^{-7}	5.56×10^{-7}

Table2. Remain dose percentage within the water phantom of each simulation

	Remain dose percentage				
	No partition	2 mm SS304	2 mm Al	5 mm Glass	5 mm PMMA
140 kVp X ray	100%	28.19%	86.39%	75.63%	91.93%
140 keV γ ray	100%	76.75%	94.78%	88.12%	93.95%
511 keV γ ray	100%	91.2%	96.89%	92.78%	96.19%

as Figure 3. The maximum energy in kiloelectron volts (keV) is numerically equal to the voltage difference between the anode and the cathode in kilovolts peak (kVp). You can see that the area under the curve is significantly reduced. The partition plate as a filter, resulting in selective attenuation of lower energy photons. When an impact happens in a GATE simulation, energy is deposited along step lines. We plot the photon dosage deposition along the water phantom's depth for photons of various energy, as seen in Figure 4 to Figure 6.

Discussion

Anti-epidemic partitions are available in large and small sizes, from large office or premises partitions to small desktop partitions. Large modular partitions are also used for the rapid establishment of temporary hospitals as medical emergency sites in disasters [16]. For the large partitions, SS304 stainless steel and aluminum were chosen for this experiment. These large partitions are usually hollow sheets clad in thin metal, so the material thickness is defined as 2 mm. SAE 304 stainless steel is the most common stainless steel. The steel contains both chromium (between 18% and

20%) and nickel (between 8% and 10.5%) [17]. Numerous home and commercial products, including exhaust manifolds,

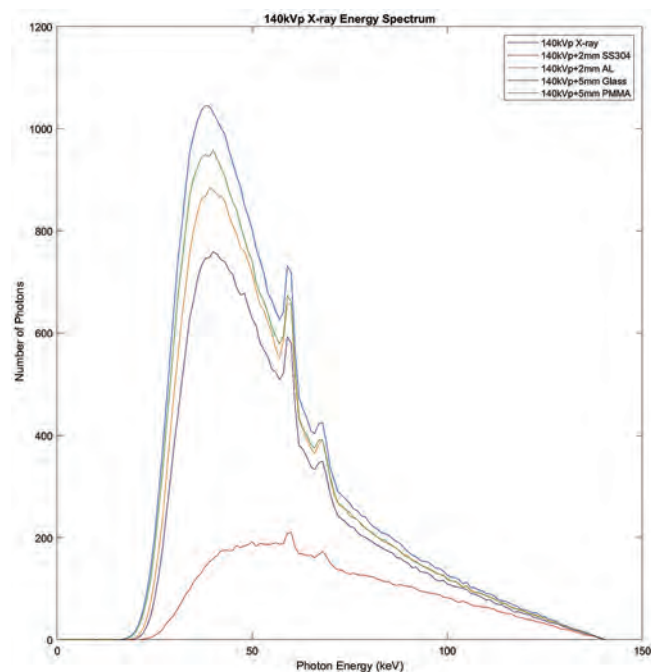


Figure 3. Simulation X-ray spectrum with and without partition shielding.

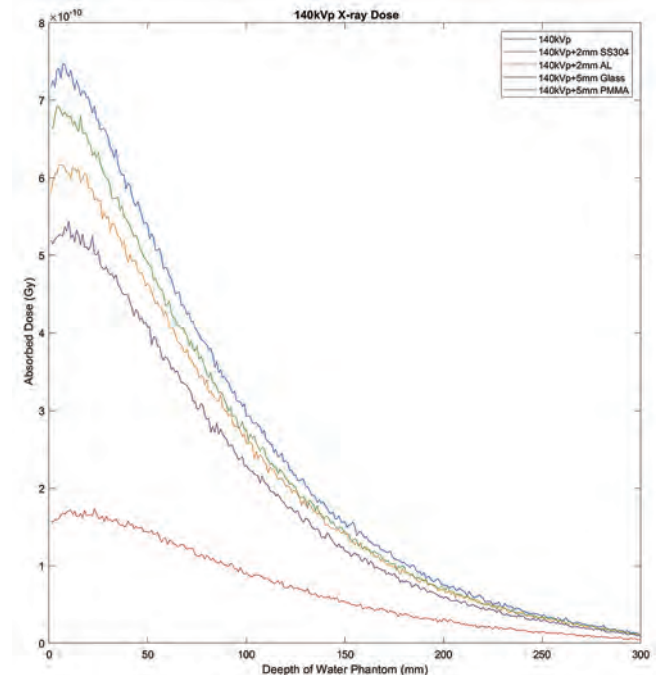


Figure 4. Variation of the absorbed dose in a simulation of 140 kVp X-ray radiation with a water phantom's depth.

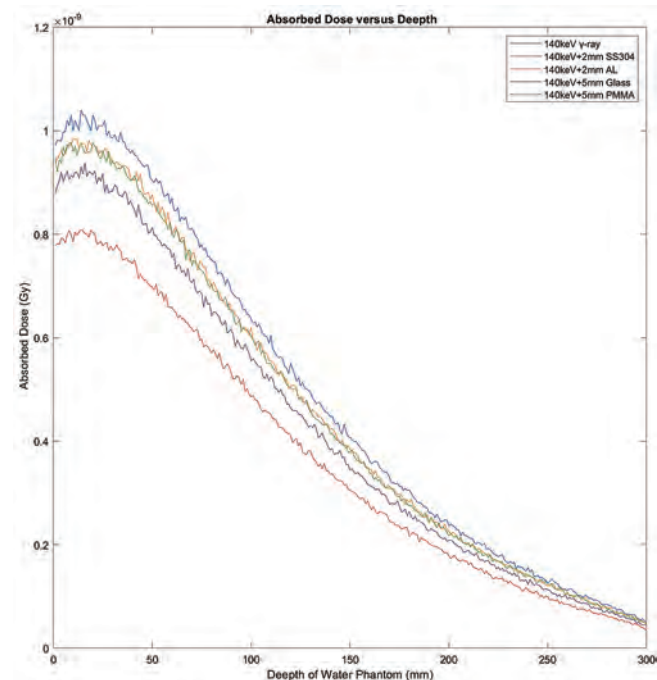


Figure 5. Variation of the absorbed dose in a simulation of 140 keV γ -ray radiation with a water phantom's depth.

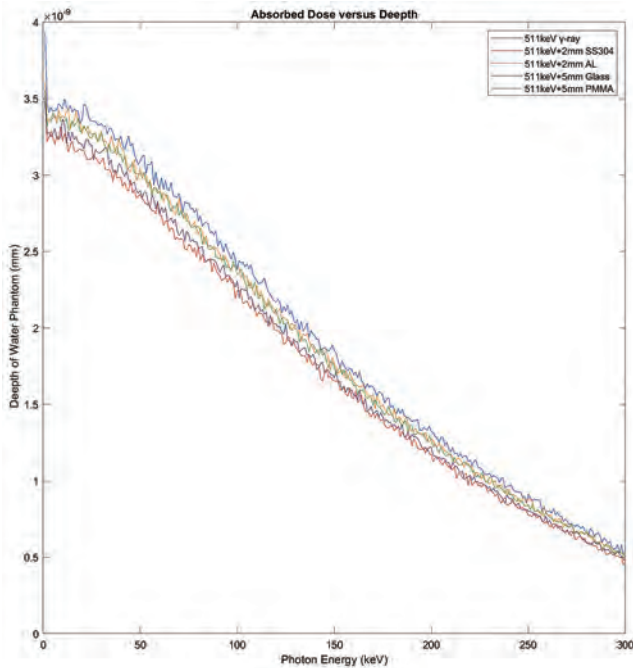


Figure 6. Variation of the absorbed dose in a simulation of 511 keV γ -ray radiation with a water phantom's depth.

screws, cutlery, and equipment for handling and processing food, are made of SS304 stainless steel. Aluminum alloys are also ideal for many industrial fabrications, allowing for stiffer and lighter designs than steel. Aluminum alloys are second only to steels in use as structural metals. 3003 aluminum alloy is commonly used in sheet metal applications such as guttering, downpipes, roofing and siding [18, 19]. As aluminum alloy is not included in the GateMaterials.db file, it was replaced by aluminum for this experiment. The density of the built-in aluminum is 2.69890 g/cm^3 , which is similar to the density of aluminum alloy (2.7 g/cm^3) [19] and about one third of SS304 steel density 7.92 g/cm^3 . From the findings of this experiment, it is evident that SS304 steel has a stronger X-ray attenuation effect than aluminum when both materials have the same thickness.

Desktop partitions are widely used in classrooms, restaurants, offices. Considering the load-bearing capacity of the desktop and the need not to block the line of sight, mostly transparent and low-density materials are used. This experiment mainly focuses on acrylic and glass. Acrylic,

often known as poly methyl methacrylate (PMMA), is a type of technical plastic. Transparent thermoplastic describes it. PMMA is also known by the trade names and brands Crylux, Plexiglas, Acrylite, Astariglas, Lucite, Perclax, and Perspex, among many others. It is also known as acrylic glass [20]. PMMA has a density of 1.19 g/cm^3 , which is very close to water and human body, and is often used as a phantom for radiation measurement [21]. Glass is an amorphous material made mostly of silica that is often transparent. Glass can be used to create optical lenses, prisms, and optoelectronic materials due to its refractive, reflecting, and transmissive qualities. General purpose glass and leaded glass for radiation protection have different densities, e.g. Corning Med-X[®] Glass has a density of 4.8 g/cm^3 [22-24]. The outcomes of this experiment demonstrate that PMMA and glass do not provide enough radiation shielding at all photon irradiation energy levels. In the routine work of the nuclear medicine department, there is a need to use partition boards that block radiation photons but are transparent, e.g. when patients are injected with radioactive tracers [25]. The effectiveness of radiation shielding depends on the ability to stop the radiation photons (particles), which varies according to the type and energy of the radiation and the shielding material used. Particle radiation consists of a stream of charged or neutral particles. The least invasive particles are alpha particles (helium nuclei), a sheet of paper can stop even very high-energy alpha particles; whereas beta particles (electrons) are more invasive, they can still be absorbed by a few millimeters of aluminum. Common anti-epidemic partitions can effectively block these particle radiations. However, photon radiations are routinely used in hospitals. Photon radiation shielding requires high atomic number and high-density materials [26]. These anti-epidemic partition materials are not effective at blocking γ -ray and X-ray. Don't have a false sense of security because of the anti-epidemic partitions; instead, staffs in the medical radiation departments should be aware of this fact. If opaque partitions are used, staffs cannot see the radiation source behind the partition, and may be exposed to accidental radiation exposure.

Conclusion

The results of this simulation show that 2 mm SS304 stainless steel has a better radiation shielding efficiency against X-rays reducing the radiation dose by approximately 70%. All other materials failed to achieve the desired radiation shielding effect at all photon energies. Among of the transparent materials, glass provide better shielding than acrylic at all photon energies. Metal and plastic partitions do not offer adequate shielding efficiency at 511 keV photon irradiation. X-ray machines and computed tomography scanners in the radiology and nuclear medicine departments are installed in rooms with radiation safety assessments. The isotope tracers used in nuclear medicine are higher in energy than normal diagnostic X-rays, and this experiment confirms that common barrier materials are inefficient in shielding these high-energy photons from radiation. Staff working in the Nuclear Medicine and Positron Emission Tomography departments should still be aware of the TDS-principals (time, distance, and shielding) and radioactive source management.

References

1. World Health Organization, *Transmission of SARS-CoV-2: implications for infection prevention precautions: scientific brief, 09 July 2020*. 2020, World Health Organization.
2. Ho, M.-J., Y.-C. Chang, and S. L. Kanter, *A SWOT analysis of medical school adaptations to COVID-19: A national survey of deans in Taiwan*. 2022.
3. Chan, J. F.-W., et al., *Surgical mask partition reduces the risk of noncontact transmission in a golden Syrian hamster model for coronavirus disease 2019 (COVID-19)*. *Clinical infectious diseases*, 2020. 71(16): p. 2139-2149.
4. Gajpal, Y., et al., *Optimal multi-stage group partition for efficient coronavirus screening*. *Annals of Operations Research*, 2022: p. 1-17.
5. Kung, C.-T., et al., *Effective strategies to prevent in-hospital infection in the emergency department during the novel coronavirus disease 2019 pandemic*. *Journal of Microbiology, Immunology, and Infection*, 2021. 54(1): p. 120.
6. Le Heron, J., et al., *Radiation protection of medical staff*. *European journal of radiology*, 2010. 76(1): p. 20-23.
7. Ferrari, P., et al., *What Is Worth Knowing in Interventional Practices about Medical Staff Radiation Exposure Monitoring: A Review of Recent Outcomes of EURADOS Working Group 12*. *Environments*, 2022. 9(4): p. 53.
8. Lee, Y., et al., *Risk perception of radiation emergency medical staff on low-dose radiation exposure: Knowledge is a critical factor*. *Journal of Environmental Radioactivity*, 2021. 227: p. 106502.
9. Rimpler, A. and I. Barth, *Beta radiation exposure of medical staff and implications for extremity dose monitoring*. *Radiation protection dosimetry*, 2007. 125(1-4): p. 335-339.
10. Cheon, B. K., et al., *Radiation safety: a focus on lead aprons and thyroid shields in interventional pain management*. *The Korean journal of pain*, 2018. 31(4): p. 244-252.
11. Jan, S., et al., *GATE: a simulation toolkit for PET and SPECT*. *Physics in Medicine & Biology*, 2004. 49(19): p. 4543.
12. Sarrut, D., et al., *Advanced Monte Carlo simulations of emission tomography imaging systems with GATE*. *Physics in Medicine & Biology*, 2021. 66(10): p. 10TR03.
13. Sarrut, D., et al., *A review of the use and potential of the GATE Monte Carlo simulation code for radiation therapy and dosimetry applications*. *Medical physics*, 2014. 41(6 Part 1): p. 064301.
14. Punnoose, J., et al., *spektr 3.0—A computational tool for x-ray spectrum modeling and analysis*. *Medical physics*, 2016. 43(8 Part 1): p. 4711-4717.
15. Siewerdsen, J., et al., *Spektr: A computational tool for x-ray spectral analysis and imaging system optimization*. *Medical physics*, 2004. 31(11): p. 3057-3067.
16. Fang, D., et al., *Large-scale public venues as medical emergency sites in disasters: lessons from COVID-19 and the use of Fangcang shelter hospitals in Wuhan*, p. 120.

- China. *BMJ global health*, 2020. 5(6): p. e002815.
17. Totten, G. E. and R. Colas, *Encyclopedia of Iron, Steel, and Their Alloys (Online Version)*. 2016: CRC Press.
 18. Sadegh, A. M. and W. M. Worek, *Marks' Standard Handbook for Mechanical Engineers, 12th Edition*. 2017: McGraw-Hill Education.
 19. Davis, J. R., *Aluminum and aluminum alloys*. 1993: ASM international.
 20. Ronco, C., *Polymethylmethacrylate: A Flexible Membrane for a Tailored Dialysis*. 1999: Karger.
 21. Shani, G., *Radiation Dosimetry Instrumentation and Methods*. 2000: Taylor & Francis.
 22. Fanderlik, I., *Silica Glass and Its Application*. 2013: Elsevier Science.
 23. Davison, S. and R. G. Newton, *Conservation and Restoration of Glass*. 2008: Taylor & Francis.
 24. Corning® Med-X® Glass. Available from: https://www.corning.com/tw/zh_tw/products/advanced-optics/product-materials/specialty-glass-and-glass-ceramics/radiation-shielding-glass/corning-med-x-glass.html.
 25. Lombardi, M. H., L. Sutton, and A. Cato, *Radiation Safety in Nuclear Medicine*. 2006: Taylor & Francis.
 26. Turner, J. E., *Atoms, Radiation, and Radiation Protection*. 2008: Wiley.

不同材質防疫隔板的輻射屏蔽能力評估： 蒙地卡羅模擬實驗

柴發順* 江泰林 歐玲君 李正輝

新光吳火獅紀念醫院 正子造影中心

中文摘要

前言：自新冠肺炎 (SARS-CoV-2) 疫情發生以來，飛沫傳染是被公認的主要傳染途徑。感染 SARS-CoV-2 主要導致呼吸道疾病，從輕度疾病到重度疾病和死亡。許多研究也顯示配戴個人防護口罩、防護衣及採用隔間隔板可以避免飛沫的傳遞，進而避免 SARS-CoV-2 的病毒傳播。在醫院的游離輻射檢查部門，例如：放射科、核子醫學科，因為動線規畫或區域分隔的需求，都廣泛的設立了分區格版。這些隔板材料包含金屬合金和塑膠聚合物。不同材質的分區隔板可以提供飛沫傳染的保護，但是對於輻射光子的遮蔽效果並不清楚。本實驗採用蒙地卡羅模擬軟體針對幾種常見的隔板材料進行模擬實驗，評估各個材料對於輻射光子的遮蔽效果。

材料與方法：使用 GATE 軟體模擬 140 kVp 的 X 光與 140 keV、511 keV 單能 γ 光子照射 $30 \times 30 \times 30$ cm 水假體。分別模擬光束直接照射，以及使用隔板屏蔽下照射 10^6 個光子的劑量分布。隔板材料包含 2 mm 厚度不鏽鋼 (SS304)、2 mm 鋁、5 mm 玻璃、5 mm 壓克力。紀錄每 1 mm 厚度水中的劑量 (Dose)，單位為格雷 (Gray, Gy)。

實驗結果：在 140 kVp 的 X 光模擬中使用 2 mm 厚度不鏽鋼、2 mm 鋁、5 mm 玻璃、5 mm 壓克力隔板的吸收劑量分別是直接照射時的 28.19%、86.39%、75.63%、91.93%。140 keV 單能 γ 光子照射模擬實驗結果為直接照射時的 76.75%、94.78%、88.12%、93.95%。511 keV 單能 γ 光子照射模擬結果為直接照射時的 91.2%、96.89%、92.78%、96.19%。

結論：本次模擬實驗結果顯示 2 mm 厚度的 SS304 不鏽鋼針對 X 光的輻射屏蔽效率較好降低了約 70% 的輻射劑量。其他材料在各個光子能量下都未能達到理想的輻射屏蔽效果。可透視材料部分玻璃在各個光子能量下都比壓克力的輻射屏蔽效果好。在 511 keV 光子照射下，無論金屬或塑膠材質隔板皆無明顯輻射屏蔽能力。核子醫學部門工作人員應注意防疫隔板並未提供明顯的輻射防護效果，以免產生不必要的輻射暴露。

關鍵詞：蒙地卡羅模擬、輻射屏蔽、隔板、GATE、Geant4

核醫技學誌 2022;19:17-24

接受日期：2022 年 9 月 15 日
通訊作者：柴發順
聯絡地址：台北市士林區文昌路 95 號 新光吳火獅紀念醫院正子造影中心
電子郵件：T005629@ms.skh.org.tw

Intestine Gastrointestinal Stromal Tumor Detected by FDG PET/CT

Ru-Hwa Cheng¹, Chi-Tai Ku^{2*}, Yen-Kung Chen^{2,3}

Department of ¹Cyclotron Center, ²Nuclear Medicine and PET Center, Shin Kong Wu Ho-Su Memorial Hospital, Taipei, Taiwan, and ³School of Medicine, Fu Jen Catholic University, New Taipei City, Taiwan

Abstract

Introduction: Gastrointestinal stromal tumor (GIST) is the most common mesenchymal tumor of the alimentary canal.

Case presentation: A 63-year-old man received fluorine-18-fluorodeoxyglucose positron emission tomography/computed tomography (FDG PET/CT) for tumor survey. He performed FDG PET/CT showing an irregular mass with heterogeneous intense FDG uptake in the pelvic cavity and a suspicious GIST with intestine involvement. Later, he received small intestine resection. Pathologic reports revealed ileum stromal cell tumor (GIST) which was high risk of malignancy.

Conclusion: FDG PET/CT provides valuable information for detection, characterization, and staging in GIST.

Key words: gastrointestinal stromal tumor, small intestine, FDG PET/CT

J Nucl Med Tech 2022;19:25-29

Introduction

Gastrointestinal stromal tumor (GIST) is the most common (80%) mesenchymal neoplasm and arising in the

muscle layer of the gastrointestinal tract [1]. GIST can occur throughout the entire gastrointestinal tract and may have extragastrintestinal involvement as well [2]. Recent studies have reported that GISTs present high malignant potential [3]. Hence, it is important to observe malignant GISTs carefully. GISTs are typically submucosal tumors, and the overlying mucosa often remains intact on pathological and imaging assessment. Preoperative evaluation of malignant GISTs remains difficult for most GISTs. It is hard to assess the stage of malignant GISTs since they are in the submucosa. Fluorine-18-fluorodeoxyglucose positron emission tomography/computed tomography (FDG PET/CT) is valuable in early detection of malignant potential in patients with GIST [4].

Case report

A 63-year-old man received FDG PET/CT for tumor survey. He has past history of 1) chin and right thigh fracture s/p operation 20 years ago, 2) ear infection s/p operation for many times. He has received four times MRI for brain, three times CT calcium score for heart, and three times FDG PET/CT (Siemens Biograph mCT) for tumor survey since 2012. Most examinations showed to be within reference limit. However, CT showed ground glass opacity (0.78 cm) in the right lung apex, without FDG uptake. This right lung ground glass opacity has stayed no change for 10 years. Prior 3rd FDG PET/CT scan was performed 5 years ago. His most recently FDG PET/CT showed an irregular mass (7.5 cm) with heterogeneous intense FDG uptake in the pelvic cavity, and a suspicious GIST with intestine involvement. Delayed FDG PET/CT scans obtained an initial phosphosoda enema

Received 2022/9/29

Corresponding author: Chi-Tai Ku

Department of Nuclear Medicine and PET Center, Shin Kong Wu Ho-Su Memorial Hospital

Address: No. 95, Wen Chang Rd., Shih Lin District, Taipei, Taiwan

Tel: 886-2-2833-2211 ext. 2280; Fax: 886-2-2838-9489

E-mail: T003744@ms.skh.org.tw

(Fleet; C.B. Fleet, Lynchburg, Va). Following evacuation, 500 mL of diluted 3% contrast medium was instilled into the anus. After anal administration of laxative-augmented contrast medium, delayed FDG PET/CT showed the lesion was not in rectosigmoid lumen. According to patient's statement, abdominal pain, melena, and body weight change were denied.

Colonoscopy showed no obvious submucosal tumor in the rectosigmoid junction in the endoscopic view. Small intestine resection was arranged and pathologic reports revealed ileum stromal cell tumor (GIST), high risk of malignancy. Tumor size: 7.5×7.3×5.5 cm. Histologic type: GIST, spindle cell type. Mitotic rate: 12/50 HPF. Immunostains result: CD117 +, Dog 1 +, SMA (smooth muscle markers) –, S-100 (nerve fiber marker) –. Pathology stage: pT3.

Discussion

GIST cases have been reported in all ages, over 90% of

GISTs occur in adults over 40 years old, in a median age of 63 years [5]. The most common location of GIST is stomach (50-60%) and small intestine (30-40%). 5-10% of GISTs arise from the colon and rectum, and 5% are located in the esophagus. Other less common locations are those outside of the gastrointestinal tract, like mesentery, retroperitoneum and omentum. There have been reported rare cases in the gallbladder, pancreas, liver and urinary bladder. In cases, where GIST occurs outside the gastrointestinal tract, the tumors are known as extragastrointestinal stromal tumors [6].

The clinical presentation of GIST 70% of the patients are symptomatic, 20% are asymptomatic and 10% are detected at autopsy. The clinical signs and symptoms are related to the presence of a mass or bleeding [7]. In this present case, patient was known with a 7.5 cm mass in pelvic and asymptomatic. GISTs have an uncertain clinical behavior ranging from small harmless tumors to aggressive, metastasizing and life-threatening sarcomas. Malignancy possibility is 20-30% [8]. This patient of GIST was found

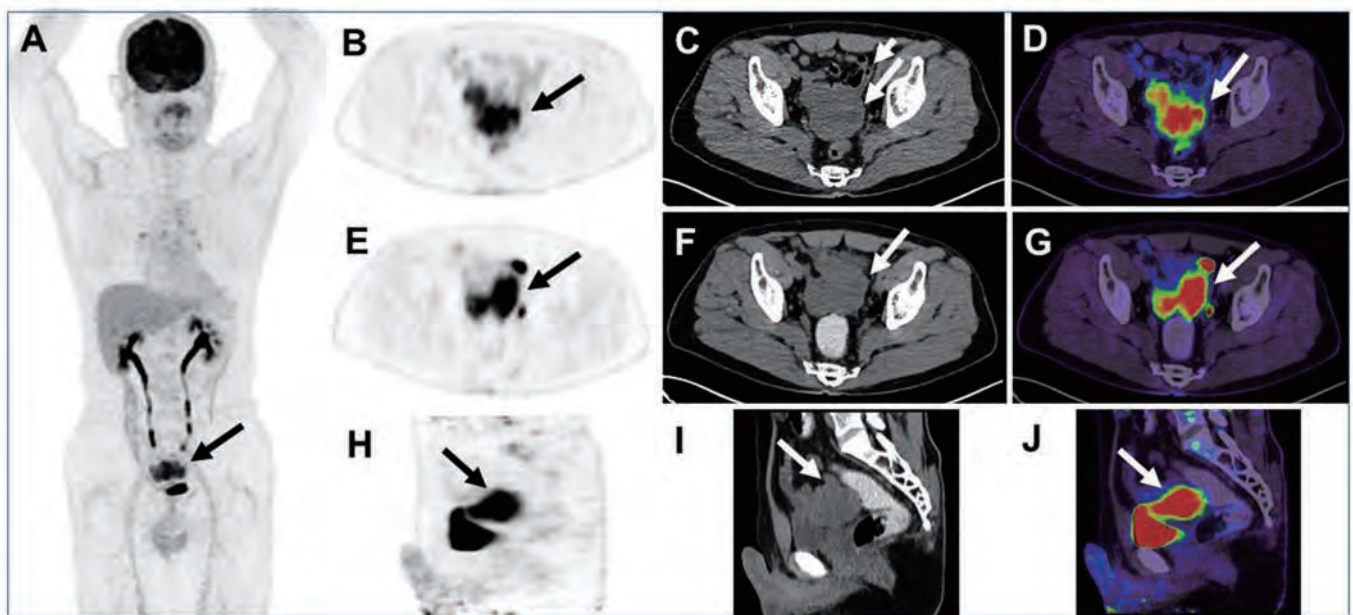


Figure 1. A 63-year-old man received FDG PET/CT for tumor survey. The arrow pointed to an irregular mass (7.5 cm, maxSUV: 12.3) with heterogeneous intense FDG uptake in the pelvic cavity (A, MIP images of PET; B, Transverse PET; C, Transverse CT; D, Transverse PET/CT fusion) with suspicious small intestine involvement (B, short arrow). Delayed FDG PET/CT scans (E, Transverse PET; F, Transverse CT; G, Transverse PET/CT fusion; H, Sagittal PET; I, Sagittal CT; J, Sagittal PET/CT fusion) obtained after anal administration of laxative-augmented contrast medium showed the lesion (arrow) was not in rectosigmoid lumen.

tumor size > 5 cm and mitotic rate > 5/50 HPF, which was considered high risk of malignancy.

GISTs are FDG-avid tumors and FDG PET-CT can be used for the initial staging and treatment response assessment. Primary GISTs are typically large, hypervascular, enhancing masses on contrast-enhanced CT scans which are often heterogeneous because of necrosis, hemorrhage, or cystic degeneration at the time of presentation [9]. A recent meta-analysis reported that FDG PET or PET/CT showed good sensitivity and specificity in predicting malignant potential of GIST [10].

The differential diagnosis for small intestinal GISTs includes primary and metastatic small intestinal neoplasms [11, 12]. Adenocarcinoma is the most common primary malignancy of the small bowel, usually appearing as an annular lesion in the proximal small intestine. Lymphoma, produces large masses within the small intestine that may ulcerate, cavity, and extend into the adjacent mesentery. Lymphoma may be indistinguishable from a GIST on radiological images, although the presence of associated lymphadenopathy would favor a diagnosis of lymphoma. The use of a laxative-augmented contrast medium before delayed FDG PET/CT is known to lead a reduction in the number of false-positive findings and increased the accuracy in the detection of colon cancer [13]. Delayed PET/CT performed after administration of a laxative augmented contrast medium might be useful for identifying patients needing additional diagnostic procedures. The rectosigmoid protocol consisted of an initial phosphosoda enema (Fleet; C.B. Fleet, Lynchburg, Va). Following evacuation, 500 mL of diluted 3% contrast medium was instilled into the anus. In this case, using laxative augmented contrast medium demonstrated that the lesion was not in the rectosigmoid.

Surgical resection of the local disease is the gold standard therapy. Its goal is to complete resection of the disease with avoidance of tumor rupture [14]. In GIST, tumor size determines the survival and regional lymph node resection has no value since GIST rarely gives rise to lymph node metastases. About 85% of GISTs are reported to have activating mutation in KIT or platelet-derived

growth factor receptor alpha (PDGFRA) [15]. Using CD117 (c-Kit), a tyrosinase kinase growth factor receptor, immunohistochemistry has proven to be a reliable and sensitive diagnostic tool [16]. With the TKI therapies against KIT and PDGFRA (imatinib and sunitinib), inoperable or metastatic GISTs are now treatable.

Conclusion

FDG PET/CT provides valuable information on detection, characterization, staging, re-staging and evaluation of response to treatment in GIST. A multiparametric evaluation based on changes in both morphological and functional data has to be assessed in GIST. PET/CT-guided management of GIST is an important example of the proof-of-the-concept of molecular imaging-based personalized medicine.

References

1. Steigen SE, Eide TJ. Gastrointestinal stromal tumors (GISTs): a review. *APMIS* 2009;117:73-86.
2. Zhao X, Yue C. Gastrointestinal stromal tumor. *J Gastrointest Oncol*. 2012;3:189-208.
3. Miettinen M, Majidi M, Lasota J. Pathology and diagnostic criteria of gastrointestinal stromal tumors (GISTs): a review. *Eur J Cancer* 2002;38:S39-51.
4. Malle P, Sorschag M, Gallowitsch HJ, et al. FDG PET and FDG PET/CT in patients with gastrointestinal stromal tumours. *Wien Med Wochenschr* 2012;162:423-9.
5. Stamatakis M, Douzinas E, Stefanaki C, et al. Gastrointestinal stromal tumor. *World J Surg Oncol*. 2009;7:61.
6. Miettinen M, Lasota J: Gastrointestinal stromal tumors - definition, clinical, histological, immunohistochemical, and molecular genetic features and differential diagnosis. *Virchows Archiv* 2001, 438:1-12.
7. Fletcher CD, Berman JJ, Corless C, et al. Diagnosis of gastrointestinal stromal tumors: A consensus approach. *Hum Pathol* 2002, 33:459-465.
8. Miettinen M, Lasota J. Gastrointestinal stromal tumors.

- Gastroenterol Clin North Am.* 2013;42:399-415.
9. Hong X, Choi H, Loyer EM, et al. Gastrointestinal stromal tumor: role of CT in diagnosis and in response evaluation and surveillance after treatment with imatinib. *Radiographics.* 2006;26:481-95.
 10. Kim SJ, Lee SW. Performance of F-18 FDG PET/CT for predicting malignant potential of gastrointestinal stromal tumors: a systematic review and meta-analysis. *J Gastroenterol Hepatol* 2018;33:576-82.
 11. Vernuccio F, Taibbi A, Picone D, et al. Imaging of Gastrointestinal Stromal Tumors: From Diagnosis to Evaluation of Therapeutic Response. *Anticancer Res.* 2016;36:2639-48.
 12. Chen SW, Chen YK, Yang TL. Intestinal GIST Mimicking as Adnexal Tumor in FDG-PET/CT Imaging. *Annals of Nuclear Medicine and Molecular Imaging* 2020;33:254-258.
 13. Chen YK, Chen JH, Tsui CC, et al. Use of Laxative-augmented Contrast Medium in the Evaluation of Colorectal Foci at FDG PET. *Radiology* 2011;259:525-533.
 14. Verweij J, Casali PG, Zalcberg J, et al. Progression-free survival in gastrointestinal stromal tumours with high-dose imatinib: randomised trial. *Lancet* 2004; 364:1127-1134.
 15. Corless CL, Fletcher JA, Heinrich MC. Biology of gastrointestinal stromal tumors. *J Clin Oncol* 2004;22:3813-25.
 16. Hornick JL, Fletcher CD. The role of KIT in the management of patients with gastrointestinal stromal tumors. *Hum Pathol* 2007;38:679-87.

氟化去氧葡萄糖正子電腦斷層造影偵測腸胃道基質瘤

鄭如華¹ 辜啓泰^{2*} 陳遠光^{2,3}

¹ 新光吳火獅紀念醫院 迴旋加速器中心

² 新光吳火獅紀念醫院 核子醫學科

³ 輔仁大學 醫學院

中文摘要

前言：腸胃道基質瘤 (GIST) 是消化道中最常見的間葉性腫瘤。

病例報告：一位 63 歲男性患者在接受了氟化去氧葡萄糖正子電腦斷層造影 (FDG PET/CT) 的腫瘤掃描後，影像的結果顯示在骨盆腔內有一氟化去氧葡萄糖不均勻攝取的不規則病灶，疑似為侵犯至小腸的腸胃道基質瘤。隨後患者接受了小腸部分切除術，病理報告證實了是迴腸基質瘤，且為高度惡性的腫瘤。

結論：氟化去氧葡萄糖正子電腦斷層造影在腸胃道基質瘤的偵測、辨識及腫瘤分期上能提供高度價值的資訊。

關鍵詞：腸胃道基質瘤、小腸、氟化去氧葡萄糖正子電腦斷層造影

核醫技學誌 2022;19:25-29

接受日期：2022 年 9 月 29 日

通訊作者：辜啓泰

聯絡地址：台北市士林區文昌路 95 號 新光吳火獅紀念醫院核子醫學科

電話：02-28332211 轉 2280；傳真：02-28389489

電子郵件：T003744@ms.skh.org.tw

利用進一步局部延遲像排除腸道 有意外發現的局部 FDG 攝取—案例報告

吳麗君¹ 楊淑琴² 顏玉安¹ 李將瑄^{1,3*}

¹ 奇美醫療財團法人奇美醫院 核醫科

² 奇美醫療財團法人柳營奇美醫院 放射腫瘤科

³ 高雄醫學大學 醫學系

中文摘要

大約 1.3-3% 的患者執行 PET/CT 中，在腸道中意外發現氟-18 去氧氟化葡萄糖局部性攝取，腸道 FDG 攝取增加的機制尚不清楚，但可能是腸道生理、炎症、良性（癌前病變）或惡性，所以意外發現腸道中的局部 FDG 攝取，不應將其僅視為生理性攝取，有可能為癌前病變 (pre-malignant) 或癌症，其比例約佔 54-70%，所以在 PET/CT 掃描發現腸道中的局部 FDG 攝取，必須施行大腸鏡。

為了提高正確性，我們報告一病人，在初期像及延遲像中，在腸道有意外發現的 FDG 局部性攝取，但在進一步局部延遲像時原先的病灶攝取消散，顯示此病灶為偽陽性，屬正常生理腸道。結論為在延遲像中連續在腸道意外發現 FDG 局部攝取的患者應執行進一步延遲成像以避免不必要的結腸鏡檢查，故特此提出報告。

關鍵詞：FDG、進一步局部延遲像、意外發現 FDG 局部攝取、正子

核醫技學誌 2022;19:31-35

前言

在接受正子放射斷層 / 電腦斷層 (positron emission

tomography/computed tomography, PET/CT) 的患者中，大約 1.3-3% 的患者在腸道中意外發現氟-18 去氧氟化葡萄糖 (fluorine-18 fluorodeoxyglucose, FDG) 局部性攝取 [1]。腸道 FDG 攝取增加的機制尚不清楚，但可能是腸道生理、炎症、良性（癌前病變）或惡性，所以意外發現腸道中的局部 FDG 攝取，不應將其僅視為生理性攝取，有可能為癌前病變 (pre-malignant) [2] 或癌症，其比例約佔 54-70% [3-5]，所以在 PET/CT 掃描發現腸道中的局部 FDG 攝取，必須施行大腸鏡。

但是我們也注意到相對有 30-46% 的病人 (100% 減去 54-70%) 是不需要做大腸鏡，如何才能鑑別真正病灶，降低不必要的侵入性大腸鏡檢查，是需要進一步去研究的。

我們報告一病人，在初期像 (initial scan) 及延遲像 (delayed scan) 中，在腸道有意外發現的 FDG 局部性攝取，而且最大標準攝取值 (maximum standardized uptake value, SUVmax) 增加 (6.15 升到 8.38)，但在進一步局部延遲像 (second delayed scan) 時原先的病灶攝取消散，SUVmax 值減少 (4.15)，顯示此病灶為偽陽性，屬正常生理腸道攝取，可避免不必要的大腸鏡，故特此提出報告。

病例報告

一位 59 歲男性病人，經上消化道鏡及病理證實為食道癌，為癌症分期安排 PET/CT 檢查。檢查前禁食 6 小時，檢查前血糖 86 mg/dl，於左手肘靜脈注射 10 mCi FDG 後，滴入 100 ml 生理食鹽水，在密閉昏暗房間內休息 60 分鐘後，執行全身初期像，從頭到腳 (含手)，因初期像顯示在腹部腸道有局部 FDG 攝取 (圖 1A)，

接受日期：2022 年 11 月 30 日

通訊作者：李將瑄

聯絡地址：71004 台南市永康區中華路 901 號 奇美醫療財團法人奇美醫院

電話：06-2812811-53575

電子郵件：chlee4@ms45.hinet.net

所以在注射後 110 分鐘後執行局部腹部延遲像 (收 3 分鐘 / 段)，延遲像顯示此處 FDG 攝取增加 (圖 1B) 並且 SUVmax 值增加 (6.15 升到 8.38)，接著在注射後 150 分鐘後執行進一步局部腹部延遲像 (收 5 分鐘 / 段)，執行進一步局部延遲像前，會請病人走動約 10-20 分、飲食、喝水，促使腸蠕動，在進一步局部延遲像顯示此病灶消散成兩處且 FDG 攝取減少 (SUV max 4.15) (圖 1C)，故判讀為偽陽性。我們使用 GE Discovery IQ PET/CT (5 環)，並搭配 Asir 低劑量 CT 及 Xeleris 影像重組軟體 (version3.1) [6-7]。

討 論

已知意外發現腸道中的局部 FDG 攝取，有可能為癌前病變或癌症，其比例約佔 54-70% [3-5]。為增加正確性，有文獻報告認為實行雙時間點 (dual-time-point) 照影，如果早期延遲相 (early delayed scanning) 及常規延遲相 (conventional delayed scanning) 時改變攝取強度及形狀 / 位置在大腸直腸處，可以正確診斷為 44% 提升 53% (14/32 提升 17/32)，但統計上無顯著差異 [8]，但我們發現診斷率提升 9% (3/32)，是不可忽視，如果可以簡單容易做進一步延遲影像提高診斷正確性是值得的。

亦有文獻認為利用 FDG 攝取增加 (SUVmax 升高)

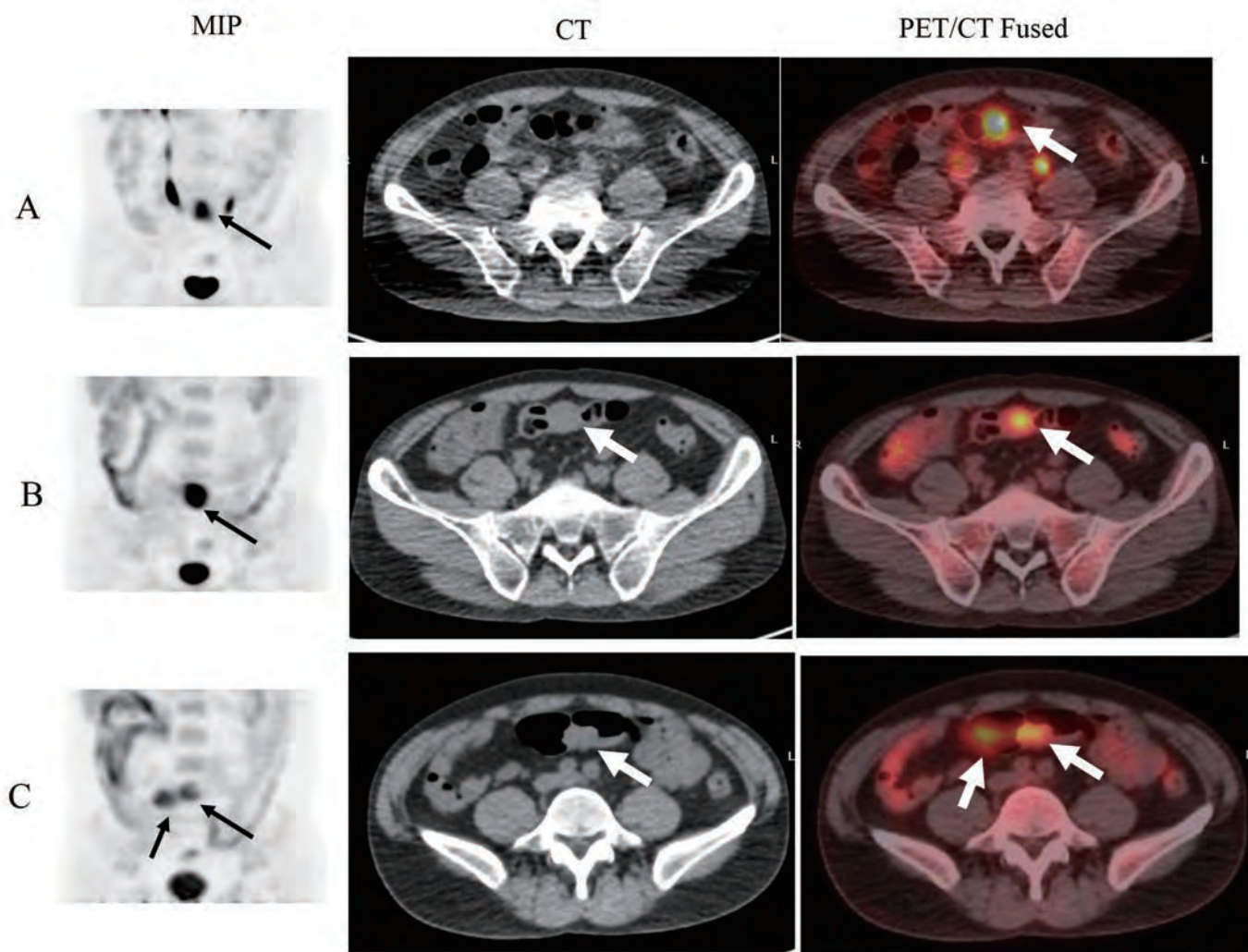


圖 1. 一個 58 歲男性食道癌病人 PET 的 MIP 和 CT 及 PET/CT Fused 影像，初期像 (A，左至右) 顯示腸道處有局部單一 FDG 攝取 (arrow)，延遲像 (B) 顯示 SUV 值增加 (6.15 升到 8.38，箭頭)，CT 上有一團軟組織，故再施行第二次局部延遲像 (C) 顯示原先局部病灶消散成二處且 SUV 值下降為 4.15 (箭頭)，故判讀為偽陽性。

能鑑別良惡性，但文獻中正常及良性 SUVmax 為 2.5 (1.2-5.2)，腺瘤及癌症分別為 2.4 (1.5-4.4) 和 4.5 (1.7-7.5)，雖有邊緣性的意義 (margin of statistical)，但重疊性太高 [9]，我們認為無法鑑別良惡性。

另有文獻提出，利用動態全身 PET (dynamic whole-body PET) 去增加腸道局部攝取的確定性可達 84% [10]，方法為每位病人連續掃四次全身造影，每次全身照影時間 3 分鐘，共需 12 分鐘，再加總 (summation) 四組全身造影成為初期影像，視腸道攝取範圍的形狀有無改變來診斷真假。我們認為此法需大量電腦運腦運算處理且要判斷五組全身影像是非常耗時，況且檢查前不知何者會有腸道意外發現，所以應不需要所有病人均施行此方法。同一家實驗室，除了原本掃動態全身 PET 外後來還加做延遲相 (delayed phase)，在初期影像相隔 40 分鐘後收取延遲像，其認為動態全身 PET 比於延遲像更有診斷價值，可以減少延遲像實行的需求 [11]。文獻中動態全身 PET 的敏感度為 95% (69/73)，而延遲像為 99% (72/73)，所以僅以動態全身 PET 會少掉 4% (3 人)。我們認為這是不可忽略，而且我們的做法是延遲像增加 3 分鐘，進一步局部延遲像增加 5 分鐘，所以是容易且可行的。

我們就只在初期全身照影有腸道局部 FDG 攝取者，做進一步局部延遲像，不需每個病人照二次全身造影，在延遲像若有腸道局部 FDG 攝取者，再做進一步局部延遲像，也不需全身造影，不僅容易實行且不必消耗大量電腦運算及判讀，如果病灶在延遲像時就消散或 SUVmax 減少，則不需加照進一步局部延遲像。

本案例我們實行初期全身照影後，意外發現在腸道有局部 FDG 攝取，FDG 攝取得相對位置在 CT 上並無軟組織團塊，有可能因 PET 與 CT 不視同時照相，有時間的延誤，導致腸蠕動位置改變，但在 PET 影像上有明顯攝取 (圖 1A，Fused)。實行延遲像後仍持續存在，且攝取增加 (SUVmax 6.15 升到 8.38，圖 1B)，CT 上有一團軟組織形狀沒改變，所以我們加照進一步局部延遲像，在進一步局部延遲像前，為使病人促進腸蠕動移動位置，會讓病人下台走動、飲食、喝水或等 20 分鐘，結果卻發現病灶消散，CT 上該團軟組織形狀改變成兩處 (圖 1C)，判定為偽陽性。

所以即使照延遲像有持續性病灶並不表示為真正病灶，進一步局部延遲像在本例證實偽陽性，最後排除病灶的可能性，也不需安排內視鏡檢查，避免侵襲性大腸

鏡檢查。

結 論

當遇到 PET/CT 的腹部腸道有局部 FDG 攝取，在延遲相時持續發現 FDG 攝取增加，可照進一步局部延遲像再次確認，則可排除偽陽性，避免侵襲性大腸鏡檢查。

參考文獻

1. Kamel, E. M.; Thumshirn, M.; Truninger, K.; Schiesser, M.; Fried, M.; Padberg, B.; Schneider, D.; Stoeckli, S. J.; von Schulthess, G. K.; Stumpe, K. D., Significance of incidental 18F-FDG accumulations in the gastrointestinal tract in PET/CT: correlation with endoscopic and histopathologic results. *Journal of nuclear medicine: official publication, Society of Nuclear Medicine* 2004, 45(11), 1804-10.
2. Kei, P. L.; Vikram, R.; Yeung, H. W.; Stroehlein, J. R.; Macapinlac, H. A., Incidental finding of focal FDG uptake in the bowel during PET/CT: CT features and correlation with histopathologic results. *AJR. American journal of roentgenology* 2010, 194(5), W401-6.
3. Kousgaard, S. J.; Gade, M.; Petersen, L. J.; Thorlacius-Ussing, O., Incidental detection of colorectal lesions on (18) F-FDG-PET/CT is associated with high proportion of malignancy: A study in 549 patients. *Endoscopy international open* 2020, 8(12), E1725-e1731.
4. Kousgaard, S. J.; Thorlacius-Ussing, O., Incidental colorectal FDG uptake on PET/CT scan and lesions observed during subsequent colonoscopy: a systematic review. *Techniques in coloproctology* 2017, 21(7), 521-529.
5. Treglia, G.; Taralli, S.; Salsano, M.; Muoio, B.; Sadeghi, R.; Giovanella, L., Prevalence and malignancy risk of focal colorectal incidental uptake detected by (18) F-FDG-PET or PET/CT: a meta-analysis. *Radiology and oncology* 2014, 48(2), 99-104.
6. Boellaard, R.; Delgado-Bolton, R.; Oyen, W. J.; Giammarile, F.; Tatsch, K.; Eschner, W.; Verzijlbergen, F. J.; Barrington, S. F.; Pike, L. C.; Weber, W. A.; Stroobants, S.; Delbeke, D.; Donohoe, K. J.; Holbrook,

- S.; Graham, M. M.; Testanera, G.; Hoekstra, O. S.; Zijlstra, J.; Visser, E.; Hoekstra, C. J.; Pruim, J.; Willemsen, A.; Arends, B.; Kotzerke, J.; Bockisch, A.; Beyer, T.; Chiti, A.; Krause, B. J., FDG PET/CT: EANM procedure guidelines for tumour imaging: version 2.0. *European journal of nuclear medicine and molecular imaging* 2015, 42(2), 328-54.
7. Yen, Y. A.; Huang, W. S.; Chiu, C. H.; Tyan, Y. C.; Wang, J. J.; Wu, L. C.; Feng, I. J.; Lee, C. H., Does Routine Triple-Time-Point FDG PET/CT Imaging Improve the Detection of Liver Metastases? *Diagnostics (Basel, Switzerland)* 2020, 10(9).
8. Miyake, K. K.; Nakamoto, Y.; Togashi, K., Dual-time-point 18F-FDG PET/CT in patients with colorectal cancer: clinical value of early delayed scanning. *Annals of nuclear medicine* 2012, 26(6), 492-500.
9. Seivert, M.; Plomteux, O.; Colard, A.; Leclercq, P.; Gauthier, D.; Houbiers, G.; Dupont, P.; Demoulin, J. C.; Fontaine, F.; Namur, G.; Witvrouw, N.; Bastens, B., Endoscopic findings in case of incidental colonic uptake in PET-CT how to improve PET-CT specificity? *Acta gastro-enterologica Belgica* 2014, 77(4), 413-7.
10. Nishimura, M.; Tamaki, N.; Matsushima, S.; Kiba, M.; Kotani, T.; Bamba, C.; Nakamura, Y.; Yamada, K., Dynamic whole-body (18)F-FDG PET for differentiating abnormal lesions from physiological uptake. *European journal of nuclear medicine and molecular imaging* 2020, 47(10), 2293-2300.
11. Kotani, T.; Nishimura, M.; Tamaki, N.; Matsushima, S.; Akiyama, S.; Kanayama, T.; Bamba, C.; Tanada, Y.; Nii, T.; Yamada, K., Comparison between dynamic whole-body FDG-PET and early-delayed imaging for the assessment of motion in focal uptake in colorectal area. *Annals of nuclear medicine* 2021, 35(12), 1305-1311.

Excluded Incidental Finding of FDG Uptake in the Bowel using a Further Delayed Image – A Case Report

Li-Chun Wu¹, Shu-Chin Yang², Yu-An Yen¹, Chiang-Hsuan Lee^{1,3*}

¹Department of Nuclear Medicine, Chi Mei Medical Center, Yongkang, Tainan, Taiwan

²Department of Radiation Oncology, Chi Mei Medical Center, Liouying, Tainan, Taiwan

³School of Medicine, Kaohsiung Medical University

Abstract

Intense focal uptake of ¹⁸F-FDG in the bowel is found in approximately 1.3-3% of patients who undergo PET/CT. The mechanism reasons of increased FDG uptake in the gastrointestinal tract are unknown but may be the result of a physiologic, inflammatory, benign, or malignant process. Malignant and premalignant lesions were found in 54%-70% patients with a PET-avid lesion underwent colonoscopy. In order to promote accuracy, we reported a case of incidental finding of FDG uptake in the bowel on initial and delayed imaging that lesion resolution on further delayed imaging confirmed false positive, it was a normal physiological intestinal tract, which can avoid unnecessary colonoscopy.

Our results indicate that patients with continuously incidental colorectal FDG uptake on delayed imaging should be referred to a further delayed imaging to avoid avoid unnecessary invasive examinations, such as colonoscopy.

Key words: FDG, further delayed imaging, PET/CT, incidental finding of FDG uptake

J Nucl Med Tech 2022;19:31-35

Received 2022/11/30

Corresponding author: Chiang-Hsuan Lee

Department of Nuclear Medicine, Chi Mei Medical Center

Address: No. 901, Zhonghua Rd., Yongkang Dist., Tainan City 710, Taiwan

Tel: 06-2812811-53575; E-mail: chlee4@ms45.hinet.net

Early Abdominal Follicular Lymphoma Detected by FDG PET/CT

Yen-Lu Lin¹, Shu-Hui Lin-Sung², Yen-Kung Chen^{2,3*}

¹United Safety Medical Group, New Taipei City, Taiwan

²Department of Nuclear Medicine and PET Center, Shin Kong Wu Ho-Su Memorial Hospital, Taipei, Taiwan

³School of Medicine, Fu Jen Catholic University, New Taipei City, Taiwan

Abstract

Introduction: Follicular lymphoma is a slow-growing B cell lymphoproliferative disorder and accounts for up to 30% of all lymphomas.

Case presentation: A 58-year-old woman suffered from abdominal discomfort and anal pain. She received a series of examination, which all showed negative. FDG PET/CT showed ill-defined nodular lesions and mesenteric fatty stranding with increased FDG uptake in the abdominal cavity, further laparoscope and biopsy were arranged. Histopathology revealed follicular lymphoma. Patient received R-COP (Rituximab, cyclophosphamide, vincristine, prednisone) x 4 course, followed by radiotherapy 30.6 Gy/17fx. Three-year follow up revealed a stable condition and no new detectable lesion.

Conclusion: In early stage of patients with follicular lymphoma, FDG PET/CT scan, drug intervention and radiotherapy may improve the prognosis of disease and prevent change into high risk group of patient.

Key words: follicular lymphoma, mesenteric lymph node, FDG PET/CT

Key words: gastrointestinal stromal tumor, small intestine, FDG PET/CT

J Nucl Med Tech 2022;19:37-41

Introduction

Lymphomas are a heterogeneous group of diseases, follicular lymphoma is the second most common worldwide after diffuse large B cell lymphoma and is the most common of the clinically indolent non-Hodgkin lymphoma [1]. Nearly 20% of patients affected by follicular lymphoma entity ultimately experience treatment failure and disease progression within 2 years from diagnosis, with a 5-year overall survival of only 50% [2]. Follicular lymphoma is proved fluorine-18-fluorodeoxyglucose (FDG)-avid on positron emission tomography (PET) in 95% of the cases [3]. For suspected follicular lymphoma, wait and watch may not be a reasonable strategy. In this case, early diagnosis and management are important.

Case report

A 58-year-old woman suffered from abdominal discomfort and anal pain for one month. She had past history of hypertension under medicine control. According to patient's statement, she denied fever, night sweats, body weight change. Gynecology examination and ultrasound was normal. Urine routine and urine cytology was within normal limit. Urology examination and uroflowmetry was normal.

Received 2022/12/6

Corresponding author: Yen-Kung Chen

Department of Nuclear Medicine and PET Center, Shin Kong Wu Ho-Su Memorial Hospital

Address: No. 95, Wen Chang Rd., Shih Lin District, Taipei, Taiwan

Tel: 886-2-2833-2211 ext. 2280; Fax: 886-2-2838-9489

E-mail: M004149@ms.skh.org.tw

Chest x-ray was negative finding. Complete blood count with differential was within normal limit. Hemoglobin was 14.8 g/dL (reference: 11-16 g/dL). Biochemistry examination revealed renal function and liver function both within normal limit. At OPD, panendoscope showed mild hyperemia of gastric antrum. Several linear shallow ulcerative streaks noted at gastric body. Colonoscopy findings: mild internal hemorrhoids are noted. FDG PET/CT (Siemens Biograph mCT) showed mesenteric lymphadenitis or lymphadenopathy is suspected. So she visited to general surgery for further

laparoscope. Dissection for three different type nodules done. Histopathology revealed follicular lymphoma in mesentery lymph nodes (1.8 cm). Immunohistochemical studies of CD20, CD45RO and bcl-2 protein were done. The lesion showed prominent B cells forming follicular pattern. The neoplastic follicles revealed positive staining for bcl-2, CD20, and CD10. They revealed negative staining for CD5, CD23, Cd43 and cyclin-D1. A WHO grade 1 follicular lymphoma was considered. Further laboratory examination showed LDH 194 U/L (reference: 140-271 U/L), and beta2

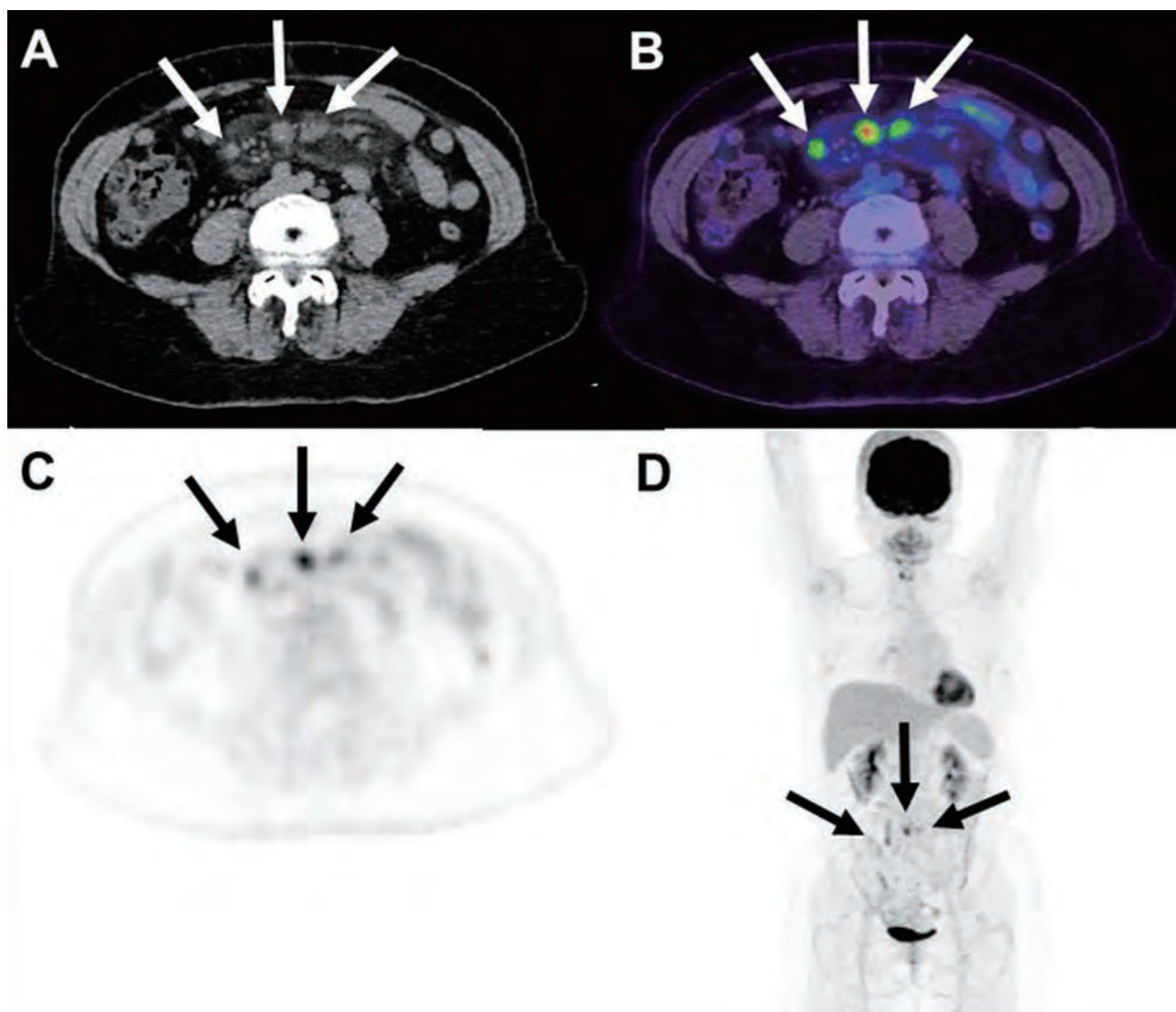


Figure 1: A 58-year-old woman had history of the abdominal discomfort and anal pain for one month. She is referred for FDG PET/CT to evaluate the extent of the disease. The arrow pointed to ill-defined nodular lesions (the largest size 2 cm) (A, Transverse CT; B, Transverse PET/CT fusion) and mesenteric fatty stranding with increased FDG uptake (C, Transverse PET; D, MIP images of PET) in the mid abdominal cavity.

microglobulin 1481 ng/mL (reference: 609-2366 ng/mL). The left iliac crest bone marrow biopsy revealed no atypical lymphoid aggregation and negative for malignancy. Under impression follicular lymphoma, grade 1. probable stage I-II. R-COP (Rituximab, cyclophosphamide, vincristine, prednisone) × 4 course was arranged, and three months later, a follow-up with FDG PET/CT scan was performed. The 2nd FDG PET/CT images revealed the pre-existing hypermetabolic mesenteric lymph nodes and mesenteric fatty infiltrations became much shrank and markedly less intense FDG uptake. Later, follow by radiotherapy 30.6 Gy/17fx. Post radiotherapy 3 months and 9 months, 3rd and 4th FDG PET/CT scan revealed the pre-existing mesenteric lymph nodes region and mesenteric fatty infiltrations became diffuse with more intense FDG uptake. Further laparoscope for mesenteric biopsy and pathology reporter showed necrosis and fibrosis, and negative for malignancy. Later, follow up 3 years with CT scan 6 times revealed stable condition of pre-existing mesenteric small retroperitoneal nodes without detectable new lesion.

Discussion

Most patients with follicular lymphoma present with painless peripheral adenopathy in the cervical, axillary, inguinal, and femoral regions. Some patients present with asymptomatic large abdominal masses, with or without evidence of gastrointestinal and/or urinary tract obstruction. In this case, patient present abdominal discomfort for one month. Staging studies usually demonstrate widely disseminated disease with overt involvement of the spleen, liver, and bone marrow [4, 5]. There is no characteristic laboratory abnormality specifically associated with follicular lymphoma and despite the large tumor burden [4].

The following five adverse prognostic factors were identified and used to identify risk groups with significantly different overall survival: Beta2 microglobulin > upper limit of normal, Bone marrow involvement, Hemoglobin < 12 g/dl, the diameter of the largest involved node > 6 cm and age > 60 years. The 5-year progression-free survival based on the risk factors is as follows: Low risk (0 risk factors): 80%;

Intermediate risk (1 - 2 risk factors): 51%; High risk (3 - 5 risk factors): 19% [6, 7]. So, early diagnosis and management are important. Delayed image and biopsy to patient may increase risk factors.

According to our experience, a small (< 2 cm) focus with FDG uptake in the abdominal cavity of asymptomatic and no cancer history patient may due to mesentery adenitis, follow up is recommended. The most common causes of mesenteric lymphadenopathy are neoplastic, inflammatory, and infectious processes [8]. Mesenteric lymphadenopathy may come from metastatic malignancy. The most common malignancy resulting in mesenteric lymphadenopathy is lymphoma. Early in the course of the disease, the lymph nodes may be small and discrete. FDG PET-CT can be used to direct the site of biopsy in patients with existing FDG uptake of lymph nodes in the abdominal. If the disease progresses, the nodes often coalesce, forming a conglomerate soft-tissue mass [8]. Evidence suggests FDG-PET/CT is a standard care for staging, restaging, prognostication and radioimmunotherapy planning in patients with follicular lymphoma [9]. The use of FDG PET/CT in the evaluation of response at the end of treatment in follicular lymphoma following the indication of performing FDG PET/CT at least 3 weeks after the last chemotherapy cycle and 3 months after radiotherapy to avoid the appearance of areas of non-specific uptake related to inflammatory changes by the treatment [10]. Drug interventions have shown better outcomes than wait and watch in the treatment of follicular lymphoma [11]. In early stage disease, radiotherapy remains the standard treatment. Radiation injury triggers inflammation and stimulates fibroblasts into myofibroblasts [12]. In this patient, 3rd and 4th FDG PET/CT scan shows FDG uptake in the mesentery region due to radiation necrosis and fibrosis. We would recommend that biopsy should be considered whenever possible to exclude the false-positive case.

Conclusion

FDG PET/CT is the first choice for the diagnosis, staging, re-staging and evaluation of response to treatment in follicular lymphoma. Ill-defined nodular lesions and

mesenteric fatty stranding with increased FDG uptake in the abdominal cavity need further management. In early stage of patients with a suspicious follicular lymphoma, wait and watch strategy is not good. In addition, drug intervention and radiotherapy may improve the prognosis of disease and prevent change into high risk group of patient.

References

1. Dada R. Diagnosis and management of follicular lymphoma: a comprehensive review. *Eur J Haematol*. 2019;103:152-63.
2. Casulo C, Byrtek M, Dawson KL, et al. Early relapse of follicular lymphoma after rituximab plus cyclophosphamide, doxorubicin, vincristine and prednisone defines patients at high risk for death: an analysis from the National Lympho Care Study. *J Clin Oncol*. 2015;33:2516-22.
3. Weiler-Sagie M, Buschelev O, Epelbaum R, et al. 18F-FDG avidity in lymphoma readdressed: a study of 766 patients. *J Nucl Med*. 2010;51:25-30.
4. Martin AR, Weisenburger DD, Chan WC, et al. Prognostic value of cellular proliferation and histologic grade in follicular lymphoma. *Blood* 1995;85:3671.
5. Anderson T, Chabner BA, Young RC, et al. Malignant lymphoma. 1. The histology and staging of 473 patients at the National Cancer Institute. *Cancer* 1982;50:2699.
6. Swerdlow SH, Campo E, Pileri SA, et al. The 2016 revision of the World Health Organization classification of lymphoid neoplasms. *Blood*. 2016;127:2375-90.
7. Freedman A. Follicular lymphoma: 2015 update on diagnosis and management. *Am J Hematol*. 2015;90:1171-8.
8. Macari M, Hines J, Balthazar E, et al. Mesenteric adenitis: CT diagnosis of primary versus secondary causes, incidence, and clinical significance in pediatric and adult patients. *AJR Am J Roentgenol*. 2002;178:853-8.
9. Gallamini A., Borra A. FDG-PET scan: a new paradigm for follicular lymphoma management. *Mediterr J Hematol Infect Dis*. 2017;9:e2017029.
10. Barrington SF, Mikhaeel NG, Kostakoglu L, et al. Role of imaging in the staging and response assessment of lymphoma: consensus of the international conference on malignant lymphomas imaging working group. *J Clin Oncol*. 2014;32:3048-58.
11. Ardeshtna KM, Qian W, Smith P, et al. Rituximab versus a watch-and-wait approach in patients with advanced-stage, asymptomatic, non-bulky follicular lymphoma: an open-label randomised phase 3 trial. *Lancet Oncol*. 2014;15:424-35.
12. Straub JM, New J, Hamilton CD, et al. Radiation-induced fibrosis: mechanisms and implications for therapy. *J Cancer Res Clin Oncol*. 2015;141:1985-94.

氟化去氧葡萄糖正子電腦斷層造影 偵測早期腹部濾泡性淋巴瘤

林衍陸¹ 林宋淑惠² 陳遠光^{2,3*}

¹ 聯安醫療集團

² 新光吳火獅紀念醫院 正子斷層造影中心

³ 新光吳火獅紀念醫院 核子醫學科

中文摘要

引言：濾泡性淋巴瘤是腫瘤成長速度緩慢的 B 細胞淋巴球病變，約占淋巴瘤疾病的百分之三十左右。

個案：58 歲女性因腹部不適及肛門疼痛就醫。例行性之一般型檢查並無特殊陽性的發現。氟化去氧葡萄糖正子電腦斷層造影 (FDG PET/CT) 呈現多處模糊的結節性病灶及腸繫膜脂肪的成股相絞現象，併腹腔氟化去氧葡萄糖吸收增加的現象。腹腔鏡暨病理檢查組織病理學報告為濾泡性淋巴瘤。個案進行四個階段的化學藥物治療 (R-COP)，並進行了放射治療 (30.6 Gy/17fx)。三年期的追蹤呈現了穩定病程變化並無新病灶的發現。

結論：濾泡性淋巴瘤個案在早期接受氟化去氧葡萄糖正子電腦斷層造影檢查，進行化學藥物及放射治療，可提昇預後並避免高危險的病情變化

關鍵詞：濾泡性淋巴瘤、腸繫膜淋巴結、氟化去氧葡萄糖正子電腦斷層造影

核醫技學誌 2022;19:37-41

接受日期：2022 年 12 月 6 日

通訊作者：陳遠光

聯絡地址：台北市士林區文昌路 95 號 新光吳火獅紀念醫院核子醫學科

電話：02-28332211 轉 2280；傳真：02-28389489

電子郵件：M004149@ms.skh.org.tw

大劑量 I-131 治療甲狀腺癌病人掃描時 發現膽囊之偽陽性探討

朱秀蘭¹ 顏維徵¹ 紀雅閔¹ 繆孝謙² 游慧貞^{3*}

¹ 高雄醫學大學附設中和紀念醫院 核子醫學部

² 高雄醫學大學附設中和紀念醫院 內科部心臟血管內科

³ 高雄醫學大學附設中和紀念醫院 影像醫學部

中文摘要

本次病例報告討論一位患有乳突性甲狀腺癌之病患，於切除甲狀腺手術後給予口服 150 mCi 之 I-131，並在七天後進行掃描檢查。在平面半身掃描及靜態掃描中，發現在肝臟附近有異常的放射性活性聚集，因在平面影像上無法定位放射性活性聚集的位置，便進一步安排單光子電腦斷層 / 電腦斷層掃描術定位，藉由 SPECT/CT 的定位影像中可以確認此異常放射累積並不是在肝臟，而是位於膽囊。

關鍵詞：甲狀腺癌、碘-131 全身掃描、偽陽性、單光子電腦斷層 / 電腦斷層

核醫技學誌 2022;19:43-45

前言

碘-131 (I-131) 治療主要作為甲狀腺癌手術後的輔助性治療，其特性為副作用十分輕微，有相關報告指出，若使用劑量在 90 mCi 以上，疾病復發的比率顯著降低。且在專科醫師指示下，使用範圍在 100 到 200 mCi 的大劑量 I-131 治療手術後殘留下來的甲狀腺組織及癌細胞，也有非常顯著的效果。甲狀腺癌病患接受 I-131 治療的適應症包括：無法開刀之原發性腫瘤、頸部開刀後殘餘

之腫瘤、遠部轉移、頸部與縱膈之淋巴腺轉移、肺部轉移、以及再發甲狀腺癌 [1]。

甲狀腺癌常見於遠端器官轉移，故臨床上常透過 I-131 的全身核醫掃描，來診斷病灶轉移的狀況。因此這種檢查方式為功能性的平面影像，會有其影像判讀的限制而出現偽陽性之病灶，若進一步使用單光子電腦斷層掃描 / 電腦斷層 (Single Photon Emission Computed Tomography, SPECT/CT)，以達到更符合真實的影像品質與診斷結果。

病例報告

一位 73 歲女性患者於超音波檢查發現左側有巨大甲狀腺腫塊，確診為乳突性甲狀腺癌，因乳突性甲狀腺癌較容易經由淋巴轉移，且甲狀腺為人體較小器官，手術時不易完全清除。因此口服 I-131 就成了治療殘餘癌細胞的最佳選擇。

患者經過數週甲狀腺素停藥及低碘飲食後，於隔離病房給予 150 mCi 口服 I-131，在服用後的第七天進行 I-131 掃描檢查，以檢查是否有其他器官之轉移。在平面半身掃描中，發現除了正常聚集在甲狀腺切除的殘餘組織、鼻骨、口腔黏膜、唾液腺、腸胃道和膀胱之外，在肝臟附近有異常的放射性活性聚集 (圖一)。因在平面影像上無法定位放射性活性聚集的位置，所以便進一步搭配使用單光子電腦斷層掃描，藉由 SPECT/CT 的定位影像中可以確認並不是在肝臟，而是在膽囊中 (圖二)。

討論

全身 I-131 掃描是一種有效用於檢測分化良好的甲狀腺癌患者轉移或殘留腫瘤部位的成像方法。所以當

接受日期：2022 年 12 月 6 日
通訊作者：游慧貞
聯絡地址：高雄市三民區十全一路 100 號
電話：07-3121101 轉 7721
電子郵件：l760192@yahoo.com.tw

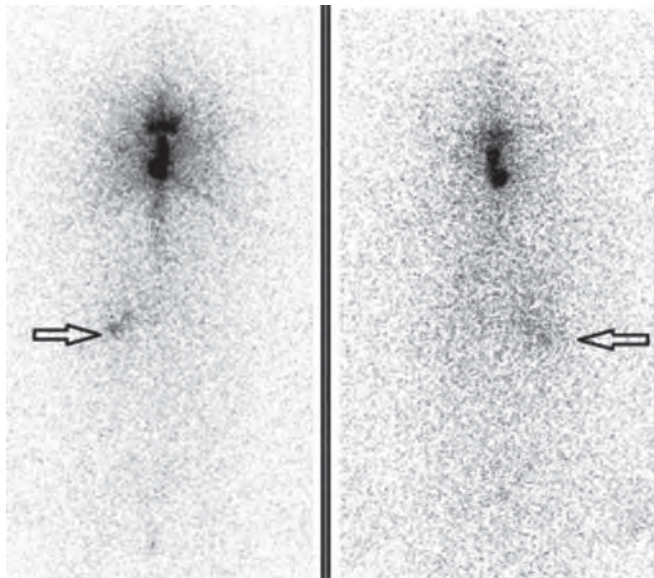


Figure 1. 在 I-131 平面半身掃描中，發現在肝臟附近有異常的放射性活性聚集。

I-131 掃描在膽囊發現異常活性時，我們曾經懷疑可能是遠端器官轉移，但透過分析此病人過往各項檢驗數據後，發現並無其他異常變化，且分化良好的甲狀腺癌轉移至膽囊的機率極低，而聚積於膽囊內的原因可能因異常膽囊型態或生理功能造成，即像是急性或慢性膽囊炎或甲狀腺功能低下造成的膽汁鬱積等等，抑或是正常膽囊也可能有放射性碘攝取。I-131 的全身掃描出現偽陽性的狀

況並非罕見，透過資料探討，發現在膽囊有異常的放射碘蓄積在國內未曾被報告過，但國外研究報告中曾有類似案例。作者描述一名甲狀腺癌患者在 I-131 掃描時也出現正常膽囊的偽陽性攝取。進行腹部超音波檢查之後，顯示膽囊沒有膽結石、炎症及轉移等狀況 [2]。

結 論

對於乳突性甲狀腺癌病患來說，利用甲狀腺癌可專一攝取 I-131 的特性，能得到相當好的治療品質。在 I-131 掃描檢查中，分化良好型甲狀腺癌轉移至遠端器官的機率並不高，但因 I-131 的全身掃描為平面影像，仍有可能出現偽陽性顯影，這時可藉由 SPECT/CT 的影像，將傳統閃爍造影機與單光子電腦斷層掃描進行影像結合，提供解剖定位更精確之融合影像，提高判讀的正確性及臨床價值。

參考文獻

1. 林昆儒、鄭如金·甲狀腺掃描與放射碘治療·*長庚醫訊*，2012；第 27 卷第七期。
2. Ju-Won Seok, Seong-Jang Kim, In-Ju Kim, Yun-Seong Kim*, Yong-Ki Kim. Normal Gallbladder Visualization during Post-Ablative Iodine-131 Scan of Thyroid Cancer. *J Korean Med Sci* 2005; 20: 521-3.

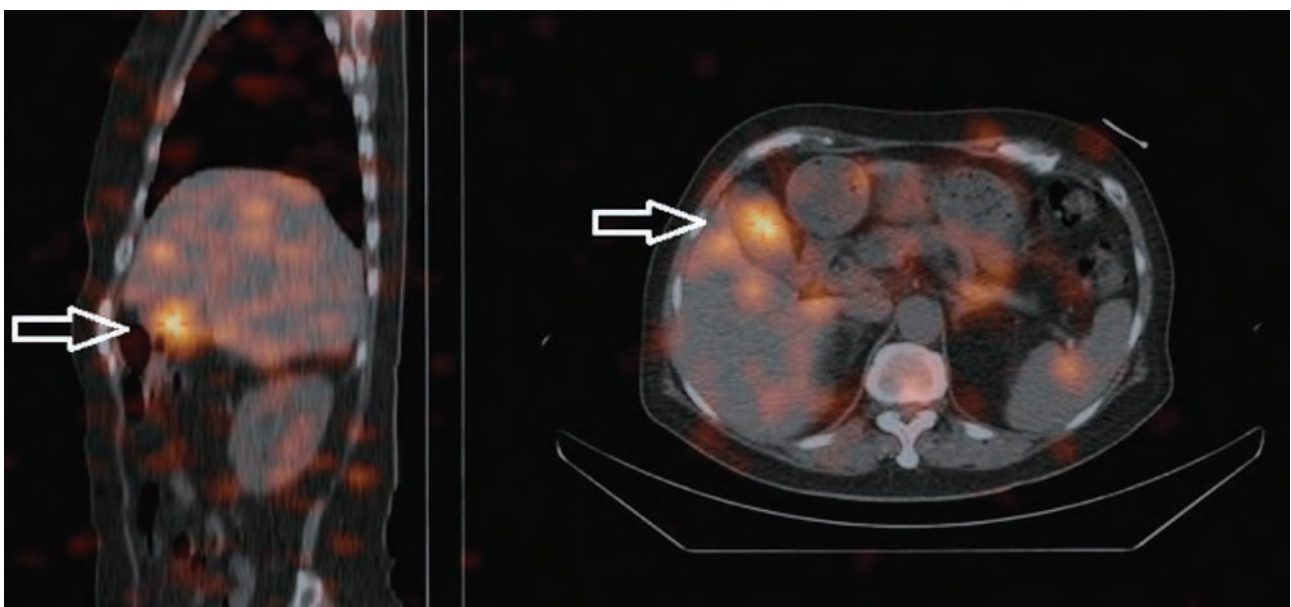


Figure 2. 在單光子電腦斷層 / 電腦斷層的影像中可確認此活性聚積並不是在肝臟，而是在膽囊中。

False Positive Uptake of Gallbladder on Whole Body Scan after High Dose Radioiodine I-131 Therapy for Differentiated Thyroid Cancer

Hsiu-Lan Chu¹, Wei-Jheng Yen¹, Ya-Min Chi¹, Hsiao-Chien Miao², Hui-Chen Yu^{3*}

¹*Department of Nuclear Medicine, Kaohsiung Medical University Hospital, Kaohsiung Medical University, Kaohsiung, Taiwan*

²*Division of Cardiology, Department of Internal Medicine, Kaohsiung Medical University Hospital, Kaohsiung Medical University, Kaohsiung, Taiwan*

³*Department of Medical Imaging, Kaohsiung Medical University Hospital, Kaohsiung Medical University, Kaohsiung, Taiwan*

Abstract

This case report presents a case of papillary thyroid cancer. The patient received radioiodine therapy with 150 mCi I-131 after total thyroidectomy. 7 days after radioiodine therapy, the patient underwent whole body scan to detect iodine absorption. Abnormal avidity near liver was found at planar scintigraphy and static scan. To better localize the avidity, SPECT/CT was done, which confirmed this abnormal accumulation was at gallbladder rather than liver.

Key words: thyroid cancer, I-131 whole scan, false positives, SPECT/CT

J Nucl Med Tech 2022;19:43-45

Received 2022/12/6

Corresponding author: Hui-Chen Yu

Address: 100, Tzyou 1st Road, Kaohsiung, Taiwan, R.O.C

Tel: 07-3121101 ext. 7721; E-mail: l760192@yahoo.com.tw

